ANTIPSYCHOTIC DRUGS SELECTIVELY DECORRELATE LONG-RANGE INTERACTIONS IN DEEP CORTICAL LAYERS

Matthias Heindorf[1] & Georg B. Keller[1,2,3]

[1]Friedrich Miescher Institute for Biomedical Research, Basel, Switzerland
[2]Faculty of Science, University of Basel, Basel, Switzerland
[3]Lead contact, correspondence to: georg.keller@fmi.ch

Psychosis is characterized by a diminished ability of the brain to distinguish externally driven activity patterns from self-generated activity patterns. Antipsychotic drugs are a class of small molecules with relatively broad binding affinity for a variety of neuromodulator receptors that, in humans, can prevent or ameliorate psychosis. How these drugs influence the function of cortical circuits, and in particular their ability to distinguish between externally and self-generated activity patterns, is still largely unclear. To have experimental control over self-generated sensory feedback we used a virtual reality environment in which the coupling between movement and visual feedback can be altered. We then used widefield calcium imaging to determine the cell type specific functional effects of antipsychotic drugs in mouse dorsal cortex under different conditions of visuomotor coupling. By comparing cell type specific activation patterns between locomotion onsets that were experimentally coupled to self-generated visual feedback and locomotion onsets that were not coupled, we show that deep cortical layers were differentially activated in these two conditions. We then show that the antipsychotic drug clozapine disrupted visuomotor integration at locomotion onsets also primarily in deep cortical layers. Given that one of the key components of visuomotor integration in cortex is long-range cortico-cortical connections, we tested whether the effect of clozapine was detectable in the correlation structure of activity patterns across dorsal cortex. We found that clozapine as well as two other antipsychotic drugs, aripiprazole and haloperidol, resulted in a strong reduction in correlations of layer 5 activity between cortical areas and impaired the spread of visuomotor prediction errors generated in visual cortex. Our results are consistent with the interpretation that a major functional effect of antipsychotic drugs is a selective alteration of long-range layer 5 mediated communication.

INTRODUCTION

Under normal conditions, self-generated movements are coupled to sensory feedback in different modalities. Locomotion, for example, is coupled to proprioceptive feedback from muscle movements, somatosensory and auditory feedback from touching the ground, vestibular feedback

from translational acceleration, and visual feedback in the form of expanding visual flow. This coupling is key to our brain's ability to learn internal models of the world (Jordan and Rumelhart, 1992). Internal models are the transformations between cortical areas and can be used to predict the sensory consequences of movement. Hallucinations and delusions can be explained as a misconfiguration of these internal models: inaccurate predictions of the sensory consequences of movements can result in self-generated activity that is not correctly distinguished from externally driven activity (Fletcher and Frith, 2009; Frith, 2005).

Self-generated movements result in broad activation of most regions of the brain (Musall et al., 2019; Stringer et al., 2019), including some primary sensory areas like visual cortex (Keller et al., 2012; Saleem et al., 2013) where they have been shown to depend on visual context (Pakan et al., 2016). The framework of predictive processing postulates that in cortex, these movement related signals are internal model based predictions of the sensory consequences of movement that are compared to externally generated bottom-up input to compute prediction errors (Jiang and Rao, 2021; Keller and Mrsic-Flogel, 2018). Evidence for this interpretation has mainly come from the discovery of movement related prediction error responses in a variety of different cortical regions and species (Attinger et al., 2017; Audette et al., 2021; Ayaz et al., 2019; Eliades and Wang, 2008; Heindorf et al., 2018; Keller et al., 2012; Keller and Hahnloser, 2009; Stanley and Miall, 2007; Zmarz and Keller, 2016), and the observation that top-down inputs from motor areas of cortex appear to convey movement related predictions of sensory input to sensory areas of cortex (Leinweber et al., 2017; Schneider et al., 2018). The neurons on which the opposing bottom-up input and top-down prediction converge are referred to as prediction error neurons and are thought to reside primarily in layer 2/3 (L2/3) of cortex (Jordan and Keller, 2020). To complete the circuit, there also needs to be a population of neurons that integrate over prediction error responses. These are referred to as internal representation neurons. It is still unclear which cortical neuron type functions as internal representation neurons, but based on anatomical arguments it has been speculated that they can be found in deep cortical layers (Bastos et al., 2012).

In humans, externally driven and self-generated activity patterns can be experimentally separated at least partially, for example, by showing subjects a visual stimulus and later asking them to visualize the same stimulus (Le Bihan et al., 1993). This type of experiment is considerably more difficult to perform in animals. Using movement as a proxy for self-generated activity patterns, however, using a virtual environment, we can compare a condition in which self-generated and externally generated activity patterns are correlated to a condition in which they are not. In the visual system, we can use a virtual reality environment to experimentally couple or decouple locomotion from visual flow

feedback. We will refer to the former as a closed loop condition and to the latter as an open loop condition. Assuming the predictive processing model is correct, we should find differences in the activation patterns in dorsal cortex in response to locomotion onsets as a function of whether they occurred with or without coupled visual flow feedback. Both prediction error neurons as well as internal representation neurons should respond differentially. Thus, we set out to investigate whether there are differences between closed and open loop activation patterns of mouse dorsal cortex, and whether these differences are neuron type specific. If hallucinations are indeed the result of aberrant activation of internal representations, possibly as a result of misconfigured internal models, antipsychotic drugs should alter the differential activation patterns in these neurons.

RESULTS

Tlx3 positive layer 5 (L5) intratelencephalic (IT) neurons distinguished closed and open loop visuomotor coupling

To investigate neuron type specific differences in activity patterns at locomotion onsets with and without self-generated visual feedback in mouse dorsal cortex, we quantified locomotion onset activity using widefield calcium imaging (Wekselblatt et al., 2016). A GCaMP variant was expressed using either a retro-orbital injection of an AAV-PHP.eB vector (Chan et al., 2017), or a cross between a Cre line and the Ai148 GCaMP6 reporter line (Daigle et al., 2018) (see Methods; **Figure 1A**, **Table S2**). Mice expressed a GCaMP variant either brain wide (C57BL/6), or in genetically identified subsets of excitatory or inhibitory neurons using Cre driver lines. Please note, we use the term 'brain wide' here to describe an expression pattern that was determined by the intersection of the AAV-PHP.eB tropism and the expression pattern of EF1α or hSyn1 promoters but that was otherwise brain wide (see Discussion). Prior to the start of the imaging experiments, mice were implanted with a crystal skull cranial window (Kim et al., 2016). We used crystal skull preparations as we found that hemodynamic artifacts were smaller in this preparation compared to those observed in clear skull preparations (**Figures S1A and S1B**). For all experiments, mice were head fixed and free to locomote on a spherical treadmill (**Figure 1B**). Activity from dorsal cortex was imaged while mice were in a closed loop visuomotor condition, in which locomotion on the spherical treadmill controlled forward movement in a virtual corridor. Following this, mice were exposed to an open loop condition during which mice were presented with a replay of the visual flow they had self-generated in the preceding closed loop condition.

97 To test whether there are differences between closed and open loop locomotion onset responses,
98 we first compared these in mice that expressed GCaMP brain wide (C57BL/6). Consistent with
99 previous findings (Musall et al., 2019; Stringer et al., 2019), we found that locomotion onset resulted
100 in broad activation across most of dorsal cortex in both conditions (**Figure 1C**). However, comparing
101 locomotion onsets in mice that expressed GCaMP6 only in Tlx3 positive L5 IT neurons, we found that
102 the activation pattern was strikingly different between closed and open loop conditions (**Figure 1D**).
103 While locomotion onset in the open loop condition resulted in an increase in activity across dorsal
104 cortex, similar to that observed in C57BL/6 mice with brain wide GCaMP expression, locomotion
105 onset in the closed loop condition resulted in a very different activation pattern: In posterior parts of
106 dorsal cortex, the activity decreased, while in anterior parts of the dorsal cortex, the activity
107 increased. To quantify these activation patterns across mice, we selected six regions of interest:
108 primary visual cortex (V1), antero-medial secondary visual cortex (V2am), retrosplenial cortex (RSC),
109 primary motor cortex (M1), anterior cingulate cortex at the level of bregma (A24b), and secondary
110 motor cortex (M2) (**Figure 1E**). In C57BL/6 mice that expressed GCaMP brain wide, closed loop
111 locomotion onset resulted in similar activity patterns across these six regions (**Figure 1F**). This
112 activity pattern was not markedly different from that observed during locomotion onsets in an open
113 loop condition (**Figure 1G**). To quantify the contribution of visual flow onset to the closed loop
114 locomotion onset activity, we measured responses to visual flow onsets that occurred in the absence
115 of locomotion in the open loop condition (**Figure 1H**). In C57BL/6 mice with brain wide GCaMP
116 expression, visual flow onsets resulted in responses that were small compared to those observed
117 during locomotion onset, even in V1. Note that a visual flow onset is a relatively weak visual stimulus
118 compared to a drifting grating stimulus. A grating stimulus is typically composed of a gray screen or a
119 standing grating stimulus that suddenly transitions to a drifting grating, and thus the visual flow
120 undergoes a very high acceleration. A visual flow onset in an open loop condition is the replay of
121 previously self-generated visual flow and thus exhibits much lower visual flow acceleration. The
122 absence of a strong visual flow onset response in C57BL/6 mice that expressed GCaMP brain wide is
123 consistent with a high similarity of closed and open loop locomotion onset responses.

124 Different from what we found in mice that expressed GCaMP brain wide, in mice that expressed
125 GCaMP6 in Tlx3 positive L5 IT neurons, the closed loop locomotion onset patterns differed markedly
126 when compared across the six regions of interest (**Figure 1I**). Moreover, these activation patterns
127 were different from those observed during open loop locomotion onsets (**Figure 1J**). While these
128 responses could partially be explained by hemodynamic occlusion, the time course of hemodynamic
129 occlusion in Tlx3-Cre mice that expressed eGFP in L5 IT neurons was similar to that observed in

130 C57BL/6 mice that expressed eGFP brain wide and mainly resulted in a decrease of fluorescence
131 (**Figures S1C and S1D**). In Tlx3 positive L5 IT neurons, open loop visual flow onsets that occurred in
132 the absence of locomotion resulted in quantifiable responses in V1 and V2am (**Figure 1K**), but the
133 closed loop locomotion onset responses in V1 could not be explained by the sum of locomotion and
134 visual flow onset responses (**Figures S2A and S2C**). Most of the widefield signals we record here
135 likely originate in compartments in superficial layers which are composed of axons and dendrites of
136 local neurons, and long-range inputs (Allen et al., 2017) (see Discussion). To test how well the
137 widefield signals recorded in V1 reflected local somatic activity in V1, we repeated the experiments
138 using two-photon calcium imaging of somatic activity in Tlx3 positive L5 IT neurons. We found that
139 while there were differences between the responses measured with widefield imaging and those
140 measured at the soma, both for locomotion onset responses and visual responses, these differences
141 did not change our conclusions (**Figure S3**).

142 To understand whether the differences between closed and open loop locomotion onset responses
143 were unique to L5 IT neurons, we repeated these experiments and analyses for the other excitatory
144 and inhibitory cortical neuron types (**Figure S4**). For each neuron type, we quantified the similarity of
145 the activity patterns associated with closed and open loop locomotion onsets by calculating the
146 correlation coefficient between the activity traces in a window around locomotion onset (-5 s to +3
147 s) and averaging across regions of interest (see Methods). We found the highest similarity between
148 closed and open loop locomotion onsets in C57BL/6 mice that expressed GCaMP brain wide and in
149 mice that expressed GCaMP6 in PV positive interneurons, and the similarity was lowest in mice that
150 expressed GCaMP6 in Tlx3 positive L5 IT neurons (**Figures 1L and S4J**). Thus, excitatory neurons of
151 deep cortical layers exhibited the strongest differences between closed and open loop locomotion
152 related activation. The remarkable aspect of these findings is not that there are differences between
153 closed and open loop locomotion onsets, particularly in visual regions of cortex one would perhaps
154 expect to find differences, but that these differences are larger specifically in the deep cortical
155 layers.

156 To quantify how the interaction between locomotion and visual flow feedback changes across dorsal
157 cortex, we computed correlations between calcium activity and locomotion speed for each region of
158 interest, for closed and open loop conditions separately. In C57BL/6 mice that expressed GCaMP
159 brain wide, this correlation was comparable between closed and open loop conditions, was highest
160 in posterior regions of dorsal cortex, and lower in more anterior regions (**Figures 2A and 2B**). In mice
161 that expressed GCaMP6 in Tlx3 positive L5 IT neurons, the correlation between locomotion speed
162 and calcium activity in the closed loop condition was negative in posterior regions of dorsal cortex

163 and positive in anterior regions. Conversely, in open loop conditions, the correlation was positive
164 throughout dorsal cortex (**Figures 2C and 2D**). To test whether it was the coupling of visual flow that
165 resulted in a reduction of the correlation in the closed loop condition or whether the presence of an
166 uncoupled visual stimulus resulted in an increase of correlation in the open loop condition, we also
167 compared these correlations to those observed when mice were locomoting in relative darkness
168 (see Methods). In C57BL/6 mice that expressed GCaMP brain wide, the correlation of calcium activity
169 with locomotion in darkness was indistinguishable from that in closed or open loop (**Figure 2B**). In
170 mice that expressed GCaMP6 in Tlx3 positive L5 IT neurons, an interesting pattern emerged. In visual
171 regions of dorsal cortex, the correlation between locomotion speed and calcium activity in relative
172 darkness resembled that observed in open loop conditions, while in frontal regions, it resembled
173 that observed in closed loop conditions. In visual regions, the coupling of visual flow resulted in a
174 reduction of correlation, while in frontal regions the presence of an uncoupled visual stimulus
175 resulted in an increase of correlations. Thus, the difference between closed and open loop
176 conditions likely had different origins in visual and frontal regions of dorsal cortex. Overall, we
177 concluded that the coupling of locomotion and resulting visual flow feedback not only activated Tlx3
178 positive L5 IT neurons differentially but did so throughout dorsal cortex, well beyond visual regions.

179 **Visuomotor prediction errors originated in visual cortical regions and had opposing effects on Tlx3**
180 **positive L5 IT activity**

181 A consequence of the natural coupling of locomotion and visual flow feedback is that movements
182 are a good predictor of self-generated sensory feedback. In our closed loop experiments, forward
183 locomotion was a strong predictor of backward visual flow. It has been speculated that such
184 predictions are used to compute prediction errors in L2/3 of cortex (Jordan and Keller, 2020).
185 Prediction errors come in two variants: Positive prediction errors that signal more visual flow than
186 predicted and negative prediction errors that signal less visual flow than predicted (Keller and Mrsic-
187 Flogel, 2018; Rao and Ballard, 1999). To probe for negative and positive prediction error signals, we
188 quantified the responses to visuomotor mismatch events and to unexpected visual stimuli
189 (representing less and more visual flow input than expected, respectively). Visuomotor mismatch
190 was introduced by briefly (1 s) halting visual flow during self-generated feedback in the closed loop
191 condition. Visual responses were elicited by presenting full-field (covering the entire toroidal screen)
192 drifting grating stimuli to a passively observing mouse (see Methods). Please note, both types of
193 prediction errors can be probed using a variety of stimuli, but the two we are using here, in our
194 experience, are the most robust at eliciting strong responses in V1. In C57BL/6 mice that expressed
195 GCaMP brain wide, both visuomotor mismatch and grating stimuli resulted in increases of activity

196 that were strongest and appeared first in visual regions of dorsal cortex (**Figures 3A-3C and S2B**). In
197 mice that expressed GCaMP6 in Tlx3 positive L5 IT neurons, visuomotor mismatch resulted in an
198 increase of activity in V1, while grating onsets resulted in a decrease of activity in V1 (**Figures 3D-3F**
199 **and S2D**). Thus, in dorsal cortex, both mismatch and drifting grating stimuli primarily activated visual
200 cortex but resulted in opposing activation patterns in Tlx3 positive L5 IT neurons. An increase in
201 activity to negative prediction errors and a decrease to positive prediction errors would be
202 consistent with either a population of negative prediction error neurons or a type of internal
203 representation neuron (Rao and Ballard, 1999). Given that L5 neurons in V1 do not exhibit the
204 opposing influence of top-down and bottom-up inputs necessary to compute prediction errors
205 (Jordan and Keller, 2020), we speculated that Tlx3 positive L5 IT neurons might function as a type of
206 internal representation neuron.

207 **The antipsychotic drug clozapine alters visuomotor integration in L5**

208 The activation of an internal representation is the brain's best guess at what the stimuli in the
209 environment are. We speculated that the activation of such an internal representation would be
210 particularly susceptible to substances that are known to reduce illusory percepts, like antipsychotic
211 drugs. We thus quantified the changes in dorsal cortex activity associated with a single
212 intraperitoneal injection of an antipsychotic drug (clozapine). In C57BL/6 mice that expressed
213 GCaMP brain wide, we found that closed and open loop locomotion onsets were almost unaffected
214 by clozapine (**Figures 4A and 4B**), while there was a small increase in open loop visual flow onset
215 responses (**Figure 4C**). In mice that expressed GCaMP6 in Tlx3 positive L5 IT neurons, however,
216 clozapine fundamentally changed both closed and open loop locomotion onset responses. In V1,
217 both types of locomotion onset now resulted in a massive increase in activity (**Figures 4D and 4E**).
218 Conversely, open loop visual flow onset responses remained largely unchanged (**Figure 4F**). These
219 effects could not be explained by clozapine induced changes in hemodynamic occlusion (**Figure S5A**)
220 or locomotion behavior (**Figures S5B and S5C**). Clozapine also had an opposing effect on the average
221 correlation of activity with locomotion speed in Tlx3 positive L5 IT neurons. While the average
222 correlation between activity and locomotion speed was increased in C57BL/6 mice that expressed
223 GCaMP brain wide, the same measure was decreased in mice that expressed GCaMP6 in Tlx3
224 positive L5 IT neurons (**Figure S5D**). Finally, we confirmed that this effect was also present when
225 recording somatic activity in V1. Using two-photon imaging, after clozapine administration we
226 observed an increase of somatic responses during locomotion onsets that was very similar to that
227 observed with widefield imaging (**Figures S5E and S5F**). Thus, consistent with the speculation that
228 Tlx3 positive L5 IT neurons might function as internal representation neurons, clozapine exhibited a

229 substantially stronger influence on locomotion onset responses in Tlx3 positive L5 IT neurons than
230 would be expected from the effect of clozapine on brain wide responses.

231 **Antipsychotic drugs decouple long-range cortico-cortical activity**

232 L5 IT neurons are likely the primary source of long-range cortical communication (Chen et al., 2019;
233 Harris et al., 2019; Leinweber et al., 2017). Given that clozapine increased locomotion onset
234 responses in L5 IT neurons in V1, we wondered whether clozapine might more generally change the
235 long-range influence between L5 IT neurons. To investigate this possibility, we computed the
236 correlations of calcium activity between the six regions of interest across both hemispheres and all
237 recording conditions. We did this first in C57BL/6 mice that expressed GCaMP brain wide before
238 (**Figure 5A**) and after a single intraperitoneal injection of clozapine (**Figure 5B**). Overall, clozapine
239 resulted in a relatively modest decrease in correlations. On repeating this experiment in mice that
240 expressed GCaMP6 in Tlx3 positive L5 IT neurons, we found a larger decrease in correlations that
241 appeared to be stronger for regions that were further apart (**Figures 5C and 5D**). To quantify these
242 changes, we plotted the correlations as a function of linear distance between the regions as
243 measured in a top-down view of dorsal cortex (**Figure S6A**). Note, this is only an approximation of
244 the actual axonal path length between the regions. To visualize the distribution of correlations, we
245 interpolated the data and represented them as heatmaps (**Figure S6B**). The resulting representation
246 for the data from C57BL/6 mice that expressed GCaMP brain wide before and after clozapine
247 injection is shown in **Figures 6A** and **6B**, respectively. We then split the data into approximately
248 equal portions of short- and long-range correlations using a cutoff of 0.9 times the bregma-lambda
249 distance (approximately 3.8 mm). While both short- and long-range correlations were reduced, this
250 reduction was not significant in either case (**Figure 6C**). We also found no evidence of a difference
251 between short- and long-range correlation changes. In mice that expressed GCaMP6 in Tlx3 positive
252 L5 IT neurons, however, we found a significant reduction in both short- and long-range correlations
253 (**Figures 6D and 6E**), and both were more strongly reduced than in C57BL/6 mice that expressed
254 GCaMP brain wide (C57BL/6 vs Tlx3-Cre x Ai148, short-range: $p < 0.05$; long-range: $p < 10^{-5}$; rank-sum
255 test). Moreover, the reduction in activity correlations was stronger for long-range correlations than
256 it was for short-range correlations (**Figure 6F**). To control for possible clozapine induced changes in
257 hemodynamic occlusion, we repeated the experiment and analyses in Tlx3-Cre mice that expressed
258 eGFP in L5 IT neurons and found that alterations in hemodynamic occlusion could not account for
259 the decrease in correlations but resulted in a small increase of the same metric (**Figures S6C-S6E**). To
260 test whether the stress of injection, or simply passage of time, could explain the observed effects,
261 we conducted a separate set of experiments in which we injected saline in a cohort of Tlx3-Cre x

262 Ai148 mice and performed the same analysis. We found no evidence of a change in correlations with
263 saline injections (**Figures S6F-S6H**). To further dissect the spatial scale at which this decorrelation
264 occurred, we repeated the experiments in Tlx3-Cre x Ai148 mice that expressed GCaMP6 in L5 IT
265 neurons, recording calcium activity using both a widefield and a two-photon microscope. We found
266 that while the activity correlations measured with the widefield imaging decreased (**Figures S7A-**
267 **S7C**), pairwise somatic activity correlations measured by two-photon imaging did not (**Figure S7D**).
268 This is consistent with the idea that decorrelation primarily occurs for long-range interactions.
269 Finally, to confirm that the clozapine induced reduction in correlation was stronger in deep cortical
270 layers, we repeated the experiment in a population of L2/3 and L4 excitatory neurons using Cux2-
271 CreERT2 x Ai148 mice. We found that clozapine also decreased correlations of cortical activity in
272 superficial excitatory neurons (**Figure S8**). However, this reduction was significantly weaker than the
273 reduction we observed in mice that expressed GCaMP6 in Tlx3 positive L5 IT neurons (Cux2-CreERT2
274 x Ai148 vs Tlx3-Cre x Ai148, short-range: $p < 0.005$, long-range: $p < 10^{-8}$, rank-sum test). Thus,
275 administration of the antipsychotic drug clozapine resulted in a decorrelation of activity across
276 dorsal cortex that was stronger in L5 IT neurons (Tlx3) than it was in either upper layer excitatory
277 neurons (Cux2) or in the brain wide average (C57BL/6).

278 To test whether the decorrelation of the activity of L5 IT neurons is specific to clozapine or might
279 more generally be a functional signature of antipsychotic drugs, we repeated the experiments with
280 two additional antipsychotic drugs, aripiprazole and haloperidol. We found that the principal effect
281 of decorrelation of the activity patterns of Tlx3 positive L5 IT neurons was preserved with both drugs
282 (**Figures 7A-7F**). These changes in correlation were absent upon injection of a psychostimulant,
283 amphetamine (**Figures 7G-7I**). Thus, it is possible that a decrease in long-range correlations between
284 cortical L5 IT neurons might be a common mechanism of action for antipsychotic drugs.

285 Changes in the correlation between cortical regions could either be driven by changes in correlated
286 external inputs or through changes in communication between cortical regions. If antipsychotic
287 drugs primarily reduce correlations by reducing the strength of communication between cortical
288 regions, independent of whether this communication is direct or indirect, we would expect to find
289 changes in the way responses spread between cortical regions. We used visuomotor prediction error
290 responses that originated in V1 (**Figure 3**) to quantify how the spread of these responses in Tlx3
291 positive L5 IT neurons was influenced by antipsychotic drugs. The computation of negative
292 prediction errors during movement is thought to be driven by an excitatory prediction of visual flow
293 mediated by long-range cortical input from L5 neurons in regions like A24b (Leinweber et al., 2017),
294 as well as an inhibitory bottom-up visual input. By contrast, the computation of a positive prediction

295 error during passive observation is thought to be driven by an excitatory bottom-up visual input and
296 an inhibitory top-down input. Thus, we would primarily expect to find a reduction in mismatch
297 responses in L5 IT neurons and a reduction in the spread of this signal to secondary visual regions.
298 This is indeed what we observed: Mismatch responses were partially reduced in V1 and almost
299 absent in V2am after injection of antipsychotic drugs (**Figure 8A**). While responses to onsets of
300 drifting gratings were also reduced in V2am, they were overall less affected by the antipsychotic
301 drugs than mismatch responses (**Figure 8B**). These results are consistent with the interpretation that
302 antipsychotic drugs reduce lateral communication in L5. Whether this communication is mediated by
303 direct long-range connections between L5 neurons, or indirectly via other cortical neurons or
304 subcortical loops, remains to be tested.

305 **DISCUSSION**

306 When interpreting our results, it should be kept in mind that the source of the widefield imaging
307 signal in these experiments is not entirely clear and is likely a combination of somatic, dendritic, and
308 axonal signals. Given that the signal attenuation half depth in cortex is on the order of 100 µm
309 (Aravanis et al., 2007), most signals likely come from the superficial 100 µm of tissue (Allen et al.,
310 2017). In the case of the Tlx3 recordings, this would mean that we were recording a mixture of
311 axonal and dendritic signals of the Tlx3 neurons that have their soma in L5 but have a dense net of
312 axons and dendrites in L1. In the case of the brain wide expression of GCaMP using an AAV-PHP.eB
313 in C57BL/6 mice, the signals we recorded likely also include contributions from thalamic axons. In
314 addition to this, there is a hemodynamic contribution to the signal (Allen et al., 2017; Ma et al.,
315 2016; Valley et al., 2020) that is the result of varying occlusion by blood vessels. We attempted to
316 correct for the hemodynamic response using a 405 nm wavelength isosbestic illumination of
317 GCaMP6 but could not recover the hemodynamic responses measured in eGFP experiments.
318 Accurate correction likely requires calibration on eGFP measurements (Valley et al., 2020). Given
319 that hemodynamic responses should not systematically differ between different mouse lines, and
320 that in the crystal skull preparation the contribution of hemodynamic occlusion to increases in
321 fluorescence was relatively small (**Figure S1**), these hemodynamic artefacts should not substantially
322 alter our conclusions. Lastly, it should be kept in mind that responses in these widefield recordings
323 inherently reflect population averages. Assuming there is some form of lateral inhibition among
324 neurons, population averages need not reflect responses of neurons that are tuned to the specific
325 stimulus presented. For example, the suppression to grating stimuli we observed in V1 Tlx3 positive
326 L5 IT neurons could be the result of a subset of Tlx3 neurons that are strongly responsive to the
327 specific grating presented suppressing the rest of the population of Tlx3 neurons. The sum of both

328 could then result in a net decrease in calcium activity. Thus, an understanding of the mechanism that
329 results in opposing population responses of Tlx3 positive L5 IT neurons to positive and negative
330 prediction errors will require measurements with single neuron resolution.

331 In our experiments we have focused on Tlx3 positive L5 IT neurons, but given that L5 IT neurons are
332 densely connected to L5 pyramidal tract neurons (Anderson et al., 2010; Kiritani et al., 2012) and to
333 L6 neurons (Xu et al., 2016; Yamawaki and Shepherd, 2015), it is not unlikely that these neuron types
334 would follow similar patterns of activity and exhibit similar susceptibility to the influence of
335 antipsychotic drugs. In the comparison of closed and open loop locomotion onsets, we do indeed
336 find that Ntsr1 positive L6 excitatory neurons exhibit similar levels of dissimilarity as those observed
337 in Tlx3 positive L5 IT neurons (**Figure 1L**). It is possible that responses in the Ntsr1 recordings,
338 however, were noisier than those in the Tlx3 recordings (**Figure S4**), likely because of the lower
339 dendritic and axonal volume of Ntsr1 positive neurons in L1. Thus, while we have focused on the
340 Tlx3 positive L5 IT neurons mainly for reasons of experimental convenience, it is possible that both
341 the differential activation in closed and open loop locomotion onsets as well as the susceptibility of
342 long-range correlations to antipsychotic drugs is a general feature of cortical layers 5 and 6. Another
343 possibility we currently cannot entirely rule out is that the decorrelation effect we observed in Tlx3
344 positive L5 IT neurons is specific to the Tlx3-Cre mouse line. However, this seems unlikely given that
345 all mouse lines we used were maintained on the same C57BL/6 background.

346 It is still unclear what the relevant sites of action in the brain are of antipsychotic drugs.
347 Antipsychotic drugs are often antagonists of the D2 receptors, which are most strongly expressed in
348 striatum. Consequently, it is sometimes assumed that the relevant site of action of antipsychotics is
349 the striatum. Consistent with this, an increase in striatal dopamine activates auditory cortex (Maia
350 and Frank, 2017) and mediates hallucination-like perceptions in mice (Schmack et al., 2021). It is
351 intriguing, however, to speculate that the effects we observed in L5 IT neurons, which provide a
352 dominant input to striatum (Morita et al., 2019), may be an alternate site of action. While it is
353 possible that the primary site of action of the antipsychotic drugs with respect to the L5
354 decorrelation phenotype we observed is striatum, this is unlikely. Changes to striato-thalamo-
355 cortical loops could appear as changes in functional connectivity observed in cortex. However,
356 feedback from striatum to cortex is exclusively mediated through thalamus, and neither L4, the
357 primary thalamo-recipient layer in cortex, nor our brain wide recordings exhibited any of the effects
358 we saw in L5 IT neurons. Thus, the effects we saw in L5 IT neurons are either not inherited from
359 striatum or are mediated by a separate set of thalamic neurons via direct thalamic input to deep
360 cortical layers (Constantinople and Bruno, 2013; Douglas and Martin, 1991). Thalamocortical

361 collaterals in deep layers, however, come from thalamic neurons that project primarily to superficial
362 layers (Oberlaender et al., 2012). Thus, we think it is unlikely that the observed effects in L5 IT
363 neurons were inherited from striatum. Independent of whether the treatment-relevant site of action
364 of antipsychotic drugs is indeed in L5 IT neurons, or whether the observed decorrelation of activity is
365 relevant to antipsychotic potency of these drugs, we speculate that the long-range decorrelation of
366 activity could be used as a basis for a functional screen for compounds with antipsychotic efficacy.
367 Given that in the brain wide recordings the decorrelation of activity was weaker compared to that
368 observed in Tlx3 positive L5 IT neurons, it might be possible to test for similar effects in human
369 subjects using layer specific fMRI recordings (Haarsma et al., 2020).

370 A rather surprising implication of our results is that the dominant mode of coupling in cortex might
371 be lateral, not vertical. Two findings would argue for this interpretation. First, while L5 was
372 differentially activated across cortical regions during closed and open loop locomotion onsets, L2/3
373 exhibited rather limited differences. Second, antipsychotics decorrelated L5 activity but had no
374 effect on L2/3. Both findings could be explained if the long-range lateral coupling within L5 is
375 stronger than the local vertical coupling between L2/3 and L5.

376 One of the diseases treated with antipsychotic drugs is schizophrenia. It has been speculated that
377 disrupted resting-state functional connectivity in brain networks involving cortex is central to the
378 pathogenesis of schizophrenia (Li et al., 2017; Northoff and Duncan, 2016). Treatment-naïve
379 schizophrenia patients predominantly exhibit increases in resting state functional connectivity
380 between cortical regions, while medicated schizophrenia patients exhibit more balanced fractions of
381 increased and decreased functional connections (Anticevic et al., 2015; Du et al., 2021; Li et al.,
382 2017). Auditory hallucinations, one of the hallmark symptoms of schizophrenia, are associated with
383 increased activation of diverse cortical regions (Catafau et al., 1994; Dierks et al., 1999; Shergill et al.,
384 2000). Thus, it is conceivable that antipsychotic drugs counteract this by reducing the strength of
385 long-range cortical connectivity mediated by L5 IT neurons, independent of whether the increased
386 activity in schizophrenic patients is indeed driven by aberrant increases in the strength of long-range
387 cortical connections or is a consequence of an aberrant increase in the strength of striato-thalamo-
388 cortical loops. However, a direct involvement of cortical circuits in the pathogenesis of schizophrenia
389 is consistent with the glutamate hypothesis of schizophrenia. This hypothesis is based on the finding
390 that NMDA receptor antagonists induce schizophrenia-like symptoms (Moghaddam and Javitt,
391 2012), and that disturbances of NMDA and AMPA receptor related gene expression are associated
392 with schizophrenia (Harrison and Weinberger, 2005; Singh et al., 2020). In V1, it has been shown that
393 NMDA receptors are necessary during visual development to establish normal prediction error

394 signaling (Widmer and Keller, 2021). Thus, it is conceivable that a disruption of glutamatergic
395 signaling in cortex that alters the way internal representations are activated by prediction errors is
396 central to the etiology of schizophrenia. If so, we should find impairments in all domains of cortical
397 function, including sensory processing. In the case of the sensory cortex, cortical dysfunctions should
398 be apparent earlier in development, concurrent with the critical period for plasticity in sensory areas
399 of cortex. While the core symptoms of schizophrenia typically appear in late adolescence, sensory
400 processing is indeed impaired in schizophrenic patients (Javitt, 2009) and is apparent, for example, in
401 the reduction of surround suppression in V1 (Yoon et al., 2009). Interestingly, some of these
402 disturbances are detectable already during childhood as visuo-perceptual and reading anomalies in
403 some subjects that later develop schizophrenia (Parellada et al., 2017). Positive symptoms of
404 schizophrenia can be explained in a predictive processing framework of cortical function as a
405 disturbance of a prediction error based update of internal representations (Fletcher and Frith, 2009;
406 Frith, 2005). There are two types of prediction error neurons, positive and negative, and, given that
407 cortex likely implements a non-hierarchical variant of predictive processing (Garner and Keller,
408 2022), two types of internal representation neurons. One set of internal representation neurons is
409 excited by positive prediction errors and inhibited by negative prediction errors, and the other one is
410 inhibited by positive prediction errors and excited by negative prediction errors (Keller and Mrsic-
411 Flogel, 2018). Tlx3 positive L5 IT neurons exhibited opposing responses to positive and negative
412 prediction errors (**Figure 3**), and, while several different interpretations are conceivable, these
413 responses would be consistent with those of internal representation neurons. Given that the effects
414 of antipsychotic drugs are predominantly observed in L5 IT neurons, and that anesthesia is thought
415 to decouple L5 neuron soma from their apical tuft and thereby prevent conscious perception (Suzuki
416 and Larkum, 2020), we speculate that Tlx3 positive L5 IT neurons may be one type of internal
417 representation neuron and one of the functionally relevant sites of antipsychotic action.

418

419 **FIGURES**

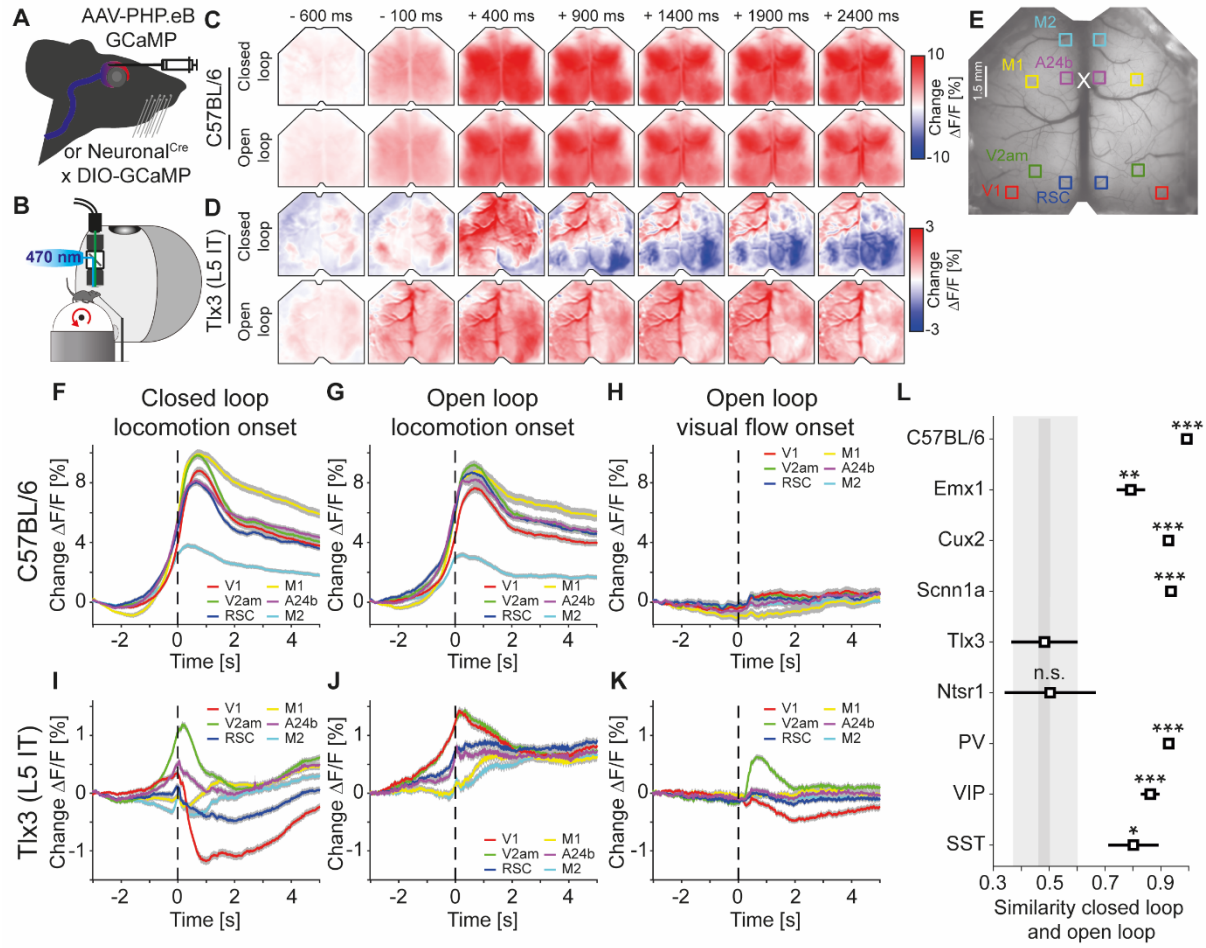

420

421 **Figure 1. Activation patterns in deep cortical layers distinguished closed and open loop locomotion**
422 **onsets more strongly than superficial layers.**

423 (**A**) Schematic of GCaMP expression strategy. We either injected an AAV-PHP.eB virus retro-orbitally
424 to express GCaMP brain wide (C57BL/6), in cortical excitatory neurons (Emx1-Cre) or in a subset of
425 SST positive interneurons (see Methods and **Table S2**), or used the progeny of a cross of a cell type
426 specific Cre driver line (Neuronal^{Cre}: Cux2-CreERT2, Scnn1a-Cre, Tlx3-Cre, Ntsr1-Cre, PV-Cre, VIP-Cre
427 or SST-Cre) with the Ai148 GCaMP6 reporter line. All mice were then implanted with a crystal skull
428 cranial window prior to imaging experiments.

429 (**B**) Schematic of the experimental setup. We imaged GCaMP fluorescence under 470 nm LED
430 illumination with an sCMOS camera through a macroscope. Mice were free to locomote on an air
431 supported spherical treadmill while coupled (closed loop), uncoupled (open loop), or no (dark) visual
432 flow in the form of movement along a virtual corridor was displayed on a toroidal screen placed in
433 front of the mouse. Walls of the virtual corridor were patterned with vertical sinusoidal gratings. In a
434 separate condition, we then presented drifting grating stimuli (grating session, see Methods).

(**C**) Average response in an example C57BL/6 mouse that expressed GCaMP6 brain wide during closed loop locomotion onsets (top row, 83 onsets) and open loop locomotion onsets (bottom row, 153 onsets). Locomotion onsets in both conditions activated dorsal cortex similarly.

(**D**) As in **C**, but in an example Tlx3-Cre x Ai148 mouse that expressed GCaMP6 in L5 IT neurons during closed loop locomotion onsets (top row, 88 onsets) and open loop locomotion onsets (bottom row, 83 onsets). Note that activity decreased in posterior regions of dorsal cortex during closed loop locomotion onsets.

(**E**) Example crystal skull craniotomy marking the 6 regions of interest in each hemisphere we selected: primary visual cortex (V1, red), retrosplenial cortex (RSC, blue), antero-medial secondary visual cortex (V2am, green), primary motor cortex (M1, yellow), anterior cingulate cortex (A24b, purple), and secondary motor cortex (M2, cyan). The white cross marks bregma.

(**F**) Average response during closed loop locomotion onsets in C57BL/6 mice that expressed GCaMP brain wide in the 6 regions of interest (907 onsets in 6 mice, activity was averaged across corresponding regions in both hemispheres). Shading indicates SEM over onsets.

(**G**) As in **F**, but for open loop locomotion onsets (598 onsets in 6 mice).

(**H**) As in **F**, but for visual flow onsets in the open loop condition restricted to times when the mice were not locomoting (416 onsets in 6 mice).

(**I**) Average response during closed loop locomotion onsets in Tlx3-Cre x Ai148 mice that expressed GCaMP6 in L5 IT neurons (1919 onsets in 15 mice, activity was averaged across corresponding regions in both hemispheres). Shading indicates SEM over onsets.

(**J**) As in **I**, but for open loop locomotion onsets (1125 onsets in 15 mice).

(**K**) As in **J**, but for visual flow onsets during open loop sessions restricted to times when the mice were not locomoting (1189 onsets in 15 mice).

(**L**) Similarity of the average closed and open loop locomotion onset responses quantified as the correlation coefficient between the two in a window -5 s to +3 s around locomotion onset (see Methods). Error bars indicate SEM over the 12 (6 per hemisphere) cortical regions. Statistical comparisons are against the Tlx3 data: n.s.: not significant, *: $p < 0.05$, **: $p < 0.01$, ***: $p < 0.001$. See **Table S1** for all information on statistical testing.

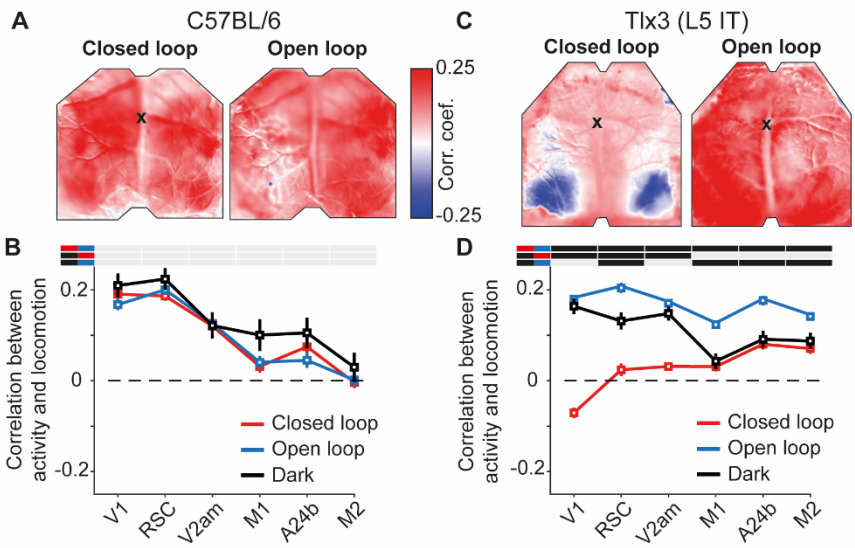

Figure 2. L5 IT neurons were differentially activated by locomotion depending on the type of visual feedback.

(**A**) Correlation between calcium activity and locomotion speed in the closed loop (left) and open loop (right) conditions, calculated for each pixel in the image for one example C57BL/6 mouse that expressed GCaMP brain wide. The black cross marks bregma. Activity in most of dorsal cortex correlates positively with locomotion speed in both closed and open loop conditions.

(**B**) Average correlation between calcium activity and locomotion speed in the 6 regions of interest in closed loop (red), open loop (blue) or dark (black) conditions in 6 C57BL/6 mice that expressed GCaMP brain wide (308, 316, and 68 5-minute sessions, respectively). Error bars indicate SEM over sessions. Bars above the plot indicate significant differences between conditions (compared conditions are indicated by colored line segments to the left, black: $p < 0.05$, gray: n.s., see **Table S1** for all information on statistical testing). On average, the correlation was highest in posterior dorsal cortex and was not different between conditions.

(**C**) As in **A**, but for an example Tlx3-Cre x Ai148 mouse that expressed GCaMP6 in L5 IT neurons. Correlations of calcium activity and locomotion speed were lower in the closed loop condition compared to the open loop condition, most prominently in posterior regions of dorsal cortex.

(**D**) As in **B**, but for 15 Tlx3-Cre x Ai148 mice that expressed GCaMP6 in L5 IT neurons (data from 420 closed loop, 394 open loop and 194 dark 5-minute sessions). Error bars indicate SEM over sessions. Correlation differed significantly between the closed and the open loop condition and was lowest in posterior dorsal cortex during the closed loop condition.

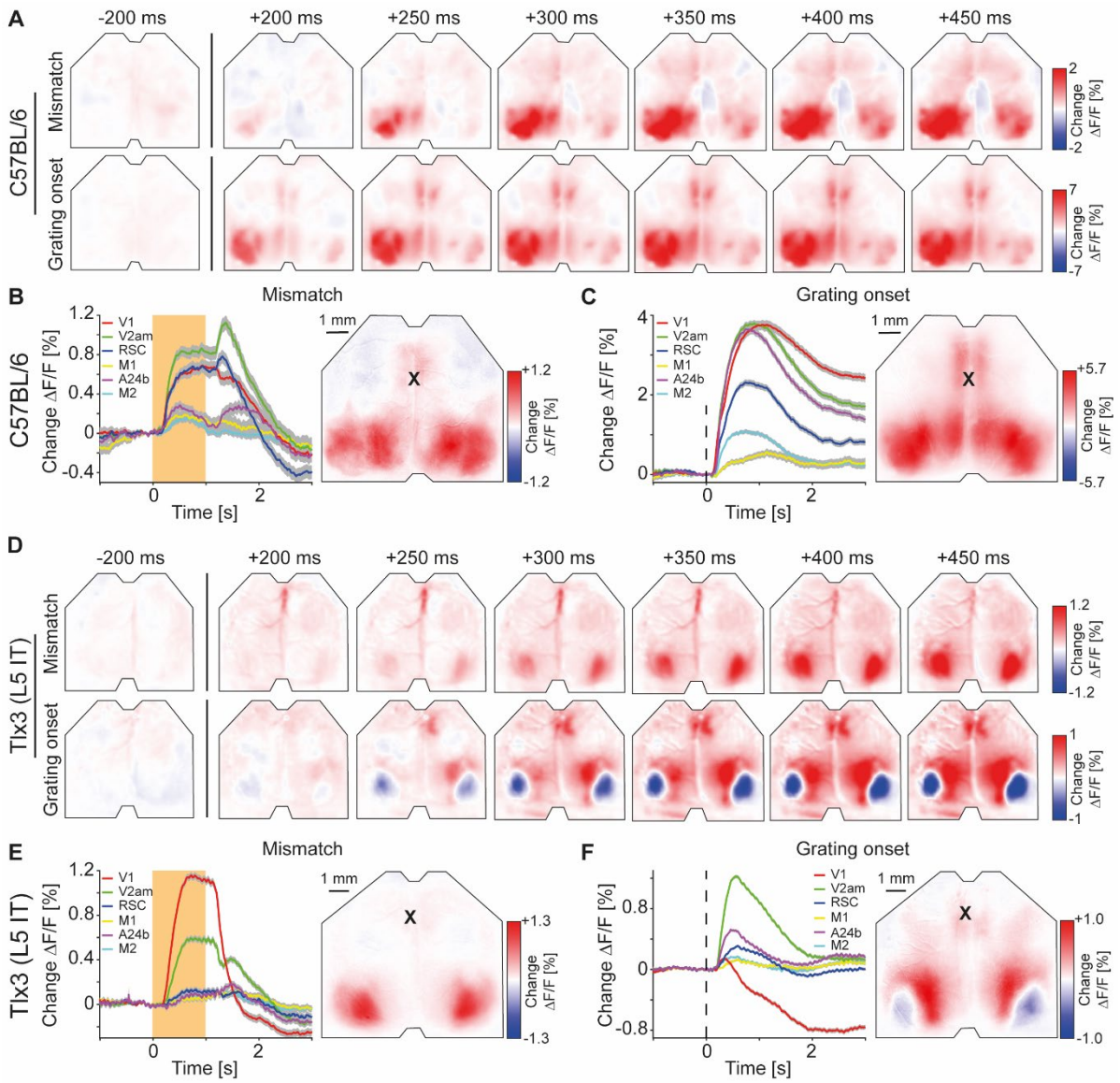

484

485 **Figure 3. Visuomotor prediction error responses in dorsal cortex originated in V1 and activated L5**
486 **IT neurons differentially.**

487 (**A**) Average responses to mismatches (top row, 230 onsets) and drifting gratings (bottom row, 86
488 onsets) in an example C57BL/6 mouse that expressed GCaMP brain wide.

489 (**B**) Left: Average response to mismatches in C57BL/6 mice that expressed GCaMP brain wide in 6
490 cortical regions (2512 onsets in 6 mice, activity was averaged across corresponding regions in both
491 hemispheres). Shading indicates SEM over onsets. Orange shading indicates duration of mismatch
492 event. Right: Average response map to mismatch in 6 C57BL/6 mice (see Methods). Black cross
493 marks bregma.

494 (**C**) As in **B**, but for drifting grating responses (1858 onsets in 6 mice).

495 (**D**) As in **A**, but in an example Tlx3-Cre x Ai148 mouse that expressed GCaMP6 in L5 IT neurons (top
496 row: mismatch, 292 onsets; bottom row: drifting gratings, 171 onsets).

(**E**) As in **B**, but for Tlx3-Cre x Ai148 mice that expressed GCaMP6 in L5 IT neurons (3297 onsets in 15 mice).

(**F**) As in **C**, but for Tlx3-Cre x Ai148 mice that expressed GCaMP6 in L5 IT neurons (5318 onsets in 15 mice).

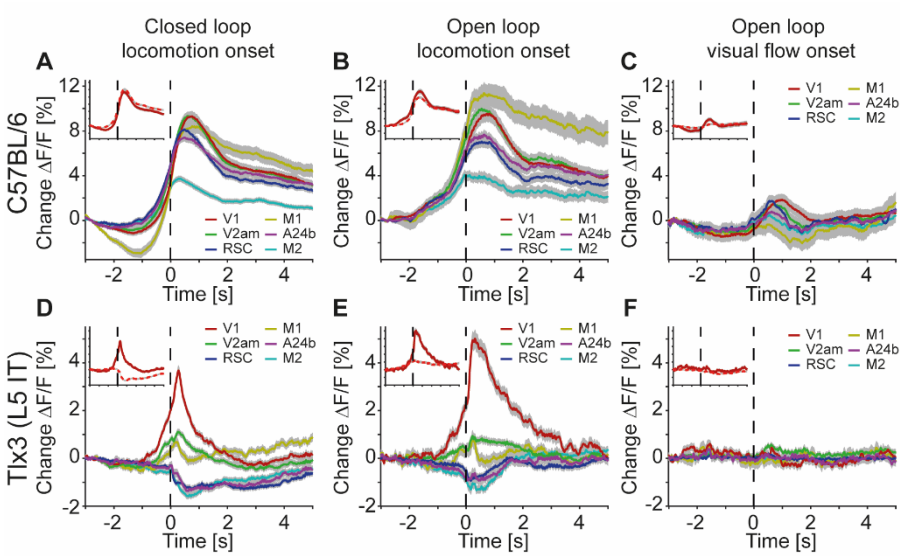

Figure 4. Clozapine increased locomotion related responses in L5 IT neurons in V1.

(**A**) Average response during closed loop locomotion onsets in C57BL/6 mice that expressed GCaMP brain wide (273 onsets in 4 mice, activity was averaged across corresponding regions in both hemispheres) after a single injection of the antipsychotic drug clozapine (see Methods). Shading indicates SEM over onsets. Inset: Comparison of responses for V1 in 4 naive C57BL/6 mice (dashed red, 720 onsets) and the same 4 mice after clozapine injection (dark red, same data as in main panel).

(**B**) As in **A**, but for open loop locomotion onsets after a clozapine injection (145 onsets in 4 mice; inset: 570 onsets in the same 4 mice before injection).

(**C**) As in **A**, but for open loop visual flow onsets restricted to times when the mice were not locomoting (99 onsets in 4 mice; inset: 404 onsets in the same 4 mice before injection).

(**D**) Average response during closed loop locomotion onsets in Tlx3-Cre x Ai148 mice that expressed GCaMP6 in layer L5 IT neurons (707 onsets in 5 mice, activity was averaged across corresponding regions in both hemispheres) after a single injection of the antipsychotic drug clozapine (see Methods). Shading indicates SEM over onsets. Inset: Comparison of responses for V1 in 5 naive Tlx3-Cre x Ai148 mice (dashed red, 1101 onsets) and the same 5 mice after clozapine injection (dark red, same data as in main panel).

(**E**) As in **D**, but for open loop locomotion onsets (350 onsets in 5 mice; inset: 348 onsets in the same 5 mice before injection).

(**F**) As in **D**, but for open loop visual flow onsets restricted to times when the mice were not locomoting (514 onsets in 5 mice; inset: 568 onsets in the same 5 mice before clozapine injection).

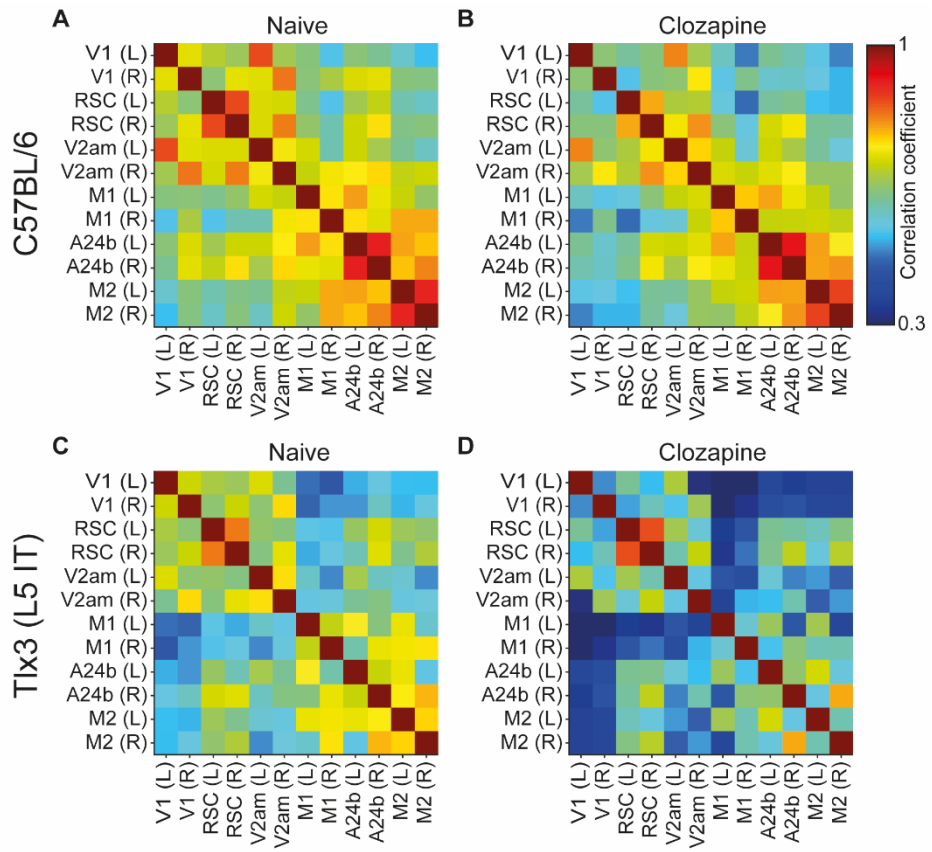

525

526 **Figure 5. Clozapine reduced activity correlations in dorsal cortex predominantly in L5 IT neurons.**

527 (**A**) Average correlation of activity between the 12 regions of interest in 4 C57BL/6 mice that
528 expressed GCaMP brain wide.

529 (**B**) As in **A**, but after a single injection of the antipsychotic drug clozapine in the same 4 C57BL/6
530 mice.

531 (**C**) Average correlation of activity between the 12 regions of interest in 5 Tlx3-Cre x Ai148 mice that
532 expressed GCaMP6 in layer L5 IT neurons.

533 (**D**) As in **C**, but after a single injection of the antipsychotic drug clozapine in the same 5 Tlx3-Cre x
534 Ai148 mice.

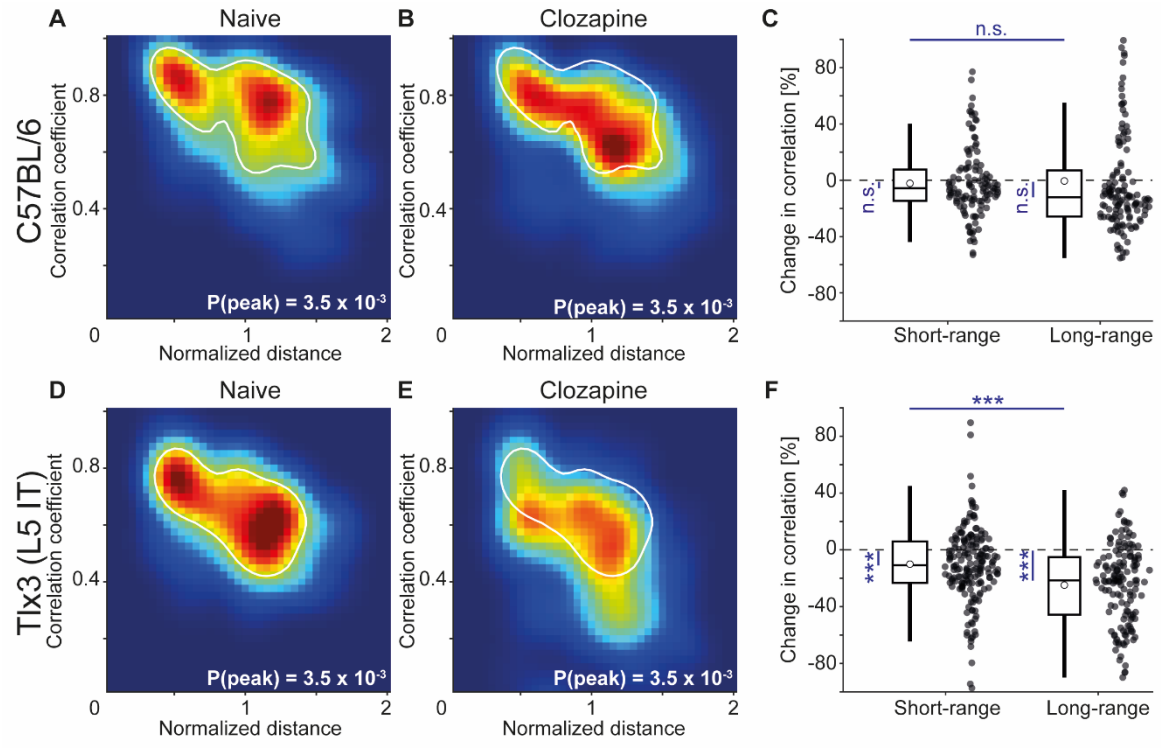

Figure 6. L5 IT neurons exhibited the strongest clozapine induced reduction of long-range correlations.

(**A**) Density map of correlation coefficients as a function of distance between the regions, normalized across mice by the bregma-lambda distance (see **Figure S6A and S6B**, and Methods), for 4 naive C57BL/6 mice that expressed GCaMP brain wide. Peak density is indicated at the bottom right of the plot and corresponds to the maximum value of the color scale (dark red). The white line is a contour line drawn at 50% of peak value.

(**B**) As in **A**, but for the same 4 C57BL/6 mice after a single injection of the antipsychotic drug clozapine. The white line is the contour line from panel **A** for comparison.

(**C**) Clozapine induced change in the activity correlation between regions, normalized to the correlation coefficient in the naive state, in 4 C57BL/6 mice. Data were split into short- and long-range activity correlations (see Methods). Boxes represent the median and the interquartile range. The open circle indicates the mean of the distribution. The whiskers mark 1.5 times the interquartile range. Dots are the individual data points (short-range: 122 pairs, long-range: 142 pairs). n.s.: not significant. See **Table S1** for all information on statistical testing.

(**D**) As in **A**, but for 5 Tlx3-Cre x Ai148 mice that expressed GCaMP6 in L5 IT neurons.

(**E**) As in **B**, but for 5 Tlx3-Cre x Ai148 mice that expressed GCaMP6 in L5 IT neurons. The white line is the contour line from panel **D** for comparison.

(**F**) As in **C**, but for 5 Tlx3-Cre x Ai148 mice that expressed GCaMP6 in L5 IT neurons (short-range: 182 pairs, long-range: 148 pairs). ***: $p < 0.001$.

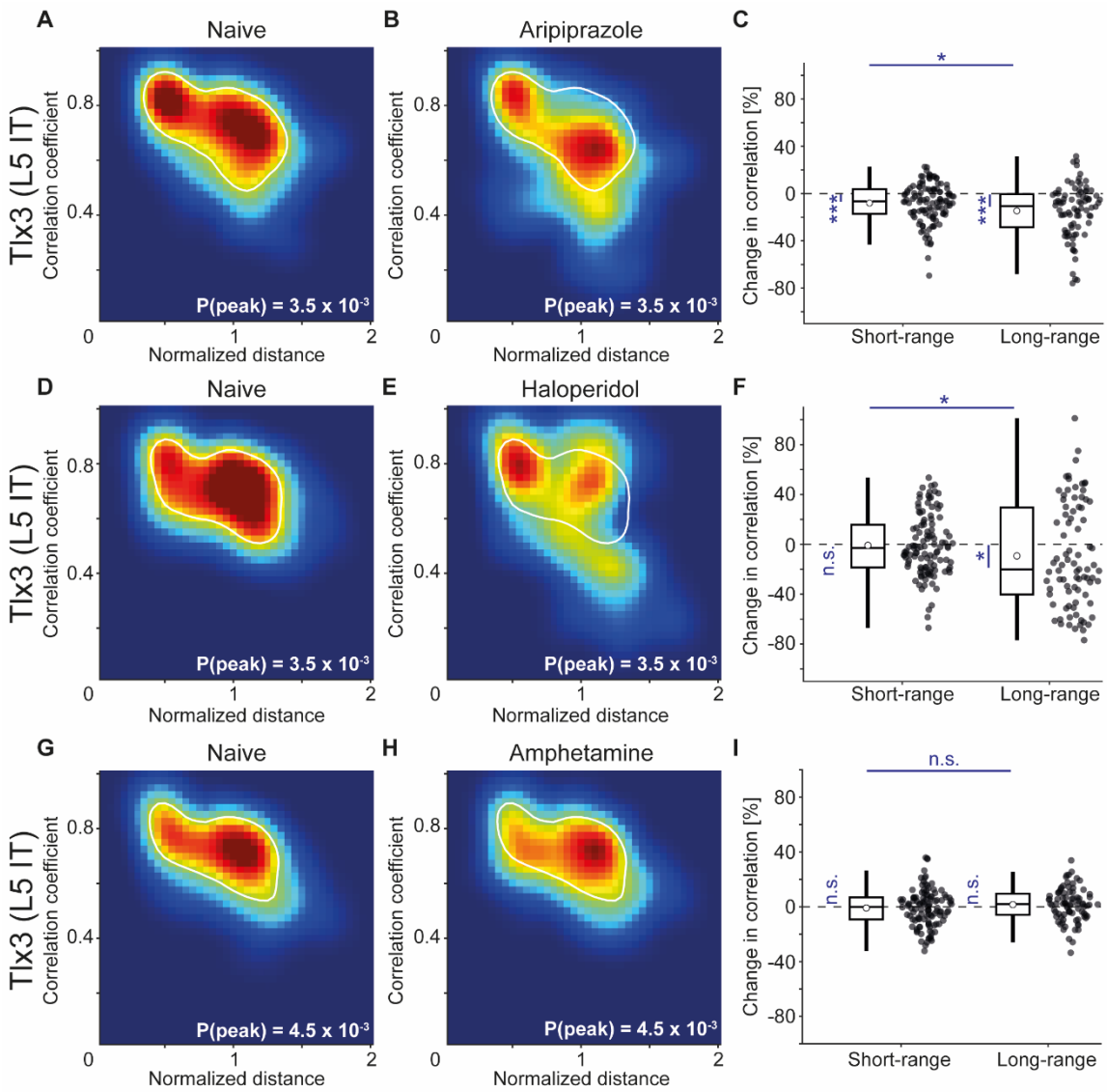

Figure 7. Antipsychotic drugs aripiprazole and haloperidol mimicked the decorrelation of L5 IT activity observed with clozapine while psychostimulant amphetamine did not.

(**A**) Density map of correlation coefficients as a function of distance between the regions, normalized across mice by the bregma-lambda distance (see **Figure S6A and S6B**, and Methods), for 3 Tlx3-Cre x Ai148 mice that expressed GCaMP6 in L5 IT neurons. Peak density is indicated at the bottom right of the plot and corresponds to the maximum value of the color scale (dark red). The white line is a contour line drawn at 50% of peak value.

(**B**) As in **A**, for the same 3 Tlx3-Cre x Ai148 mice, but after a single injection of the antipsychotic drug aripiprazole. The white line is the contour line from panel **A** for comparison.

(**C**) Aripiprazole induced change in the activity correlation between regions, normalized to the correlation coefficient in the naive state, in 3 Tlx3-Cre x Ai148 mice. Data were split into short- and long-range activity correlations (see Methods). Boxes represent the median and the interquartile range. The open circle indicates the mean of the distribution. The whiskers mark 1.5 times the

570 interquartile range. Dots are the individual data points (short-range: 114 pairs, long-range: 84 pairs).
571 *: $p < 0.05$, ***: $p < 0.001$. See **Table S1** for all information on statistical testing.

572 (**D**) As in **A**, but for 3 different Tlx3-Cre x Ai148 mice.

573 (**E**) As in **D**, for the same 3 Tlx3-Cre x Ai148 mice, but after a single injection of the antipsychotic drug
574 haloperidol. The white line is the contour line from panel **D** for comparison.

575 (**F**) As in **C**, but for the 3 mice that had received a single injection of the antipsychotic drug
576 haloperidol (short-range: 114 pairs, long-range: 84 pairs). *: $p < 0.05$; n.s.: not significant.

577 (**G**) As in **A**, but for 3 different Tlx3-Cre x Ai148 mice.

578 (**H**) As in **G**, for the same 3 Tlx3-Cre x Ai148 mice, but after a single injection of the psychostimulant
579 amphetamine. The white line is the contour line from panel **G** for comparison.

580 (**I**) As in **D**, but for the 3 mice that had received a single injection of the psychostimulant
581 amphetamine (short-range: 114 pairs, long-range: 84 pairs). n.s.: not significant.

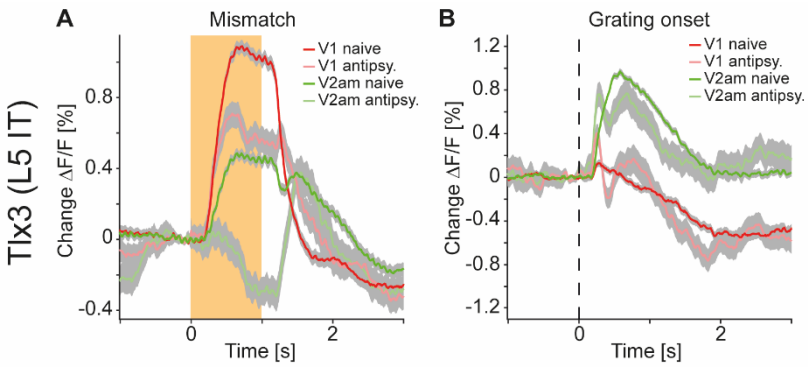

Figure 8. Antipsychotic drug treatment reduced responses to and propagation of negative prediction errors.

(**A**) Average responses to mismatches in Tlx3-Cre x Ai148 mice that expressed GCaMP6 in L5 IT neurons before (red: V1 naive, green: V2am naive, activity was averaged across corresponding regions in both hemispheres) and after (pale red: V1, pale green: V2am) injection of a single dose of an antipsychotic drug (data were averaged over all antipsychotics used: Clozapine: 5 mice, aripiprazole: 3 mice, and haloperidol: 3 mice). Orange shading indicates duration of the mismatch event. Gray shading indicates SEM over onsets (naive: 2464 onsets, antipsychotics: 2017 onsets).

(**B**) As in **A**, but for drifting grating onsets (naive: 3942 onsets, antipsychotics: 1645 onsets).

SUPPLEMENTAL FIGURES

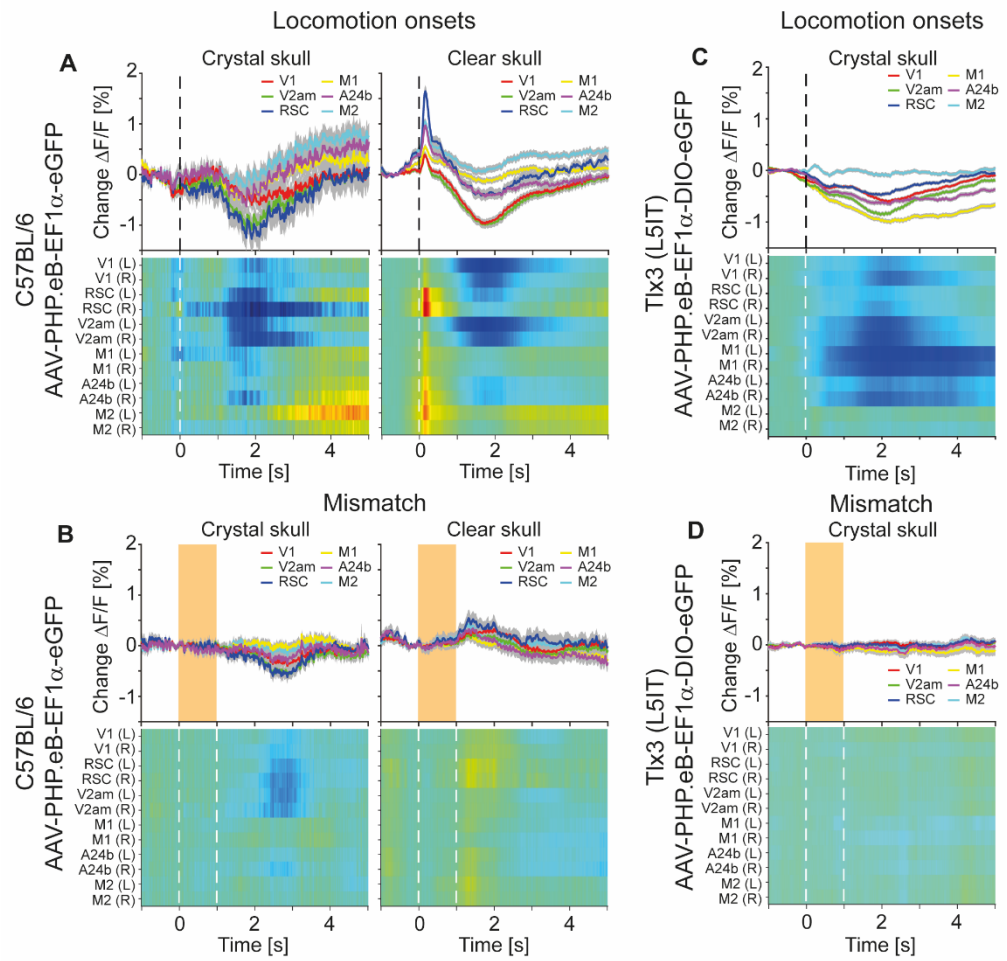

Figure S1. Fluorescence changes driven by hemodynamic occlusion. Related to Figure 1.

(**A**) Average responses during locomotion onsets in C57BL/6 mice that expressed eGFP brain wide using a crystal skull preparation (left: 3 mice, 96 locomotion onsets) or in similarly transfected mice using a clear skull preparation (right: 5 mice, 615 locomotion onsets) (see Methods). Top row shows the average activity of corresponding regions in dorsal cortex. Shading indicates SEM over onsets. The heatmaps in the bottom row show the responses for individual regions of interest. Heatmaps are scaled to the y-axis limits of the plot above (blue low, red high). Note, the fast onset transient apparent in the clear skull preparation was absent in the crystal skull preparation, while the slow decrease of activity was present in both. The increase in fluorescence at locomotion onset, which was primarily apparent in the clear skull preparation, is driven by hemodynamic occlusion.

(**B**) As in **A**, but for mismatches (left: 229 onsets in 3 mice, right: 228 onsets in 5 mice). Orange shading (top) or white dashed lines (bottom) indicate the duration of the mismatch stimulus.

(**C**) As in **A**, left, but for 7 Tlx3-Cre that had been retro-orbitally injected with an AAV-PHP.eB-DIO-eGFP to express eGFP in L5 IT neurons (1880 onsets).

608 (**D**) As in **B**, left, but for 7 Tlx3-Cre that had been retro-orbitally injected with an AAV-PHP.eB-DIO-
609 eGFP to express eGFP in L5 IT neurons (451 onsets).

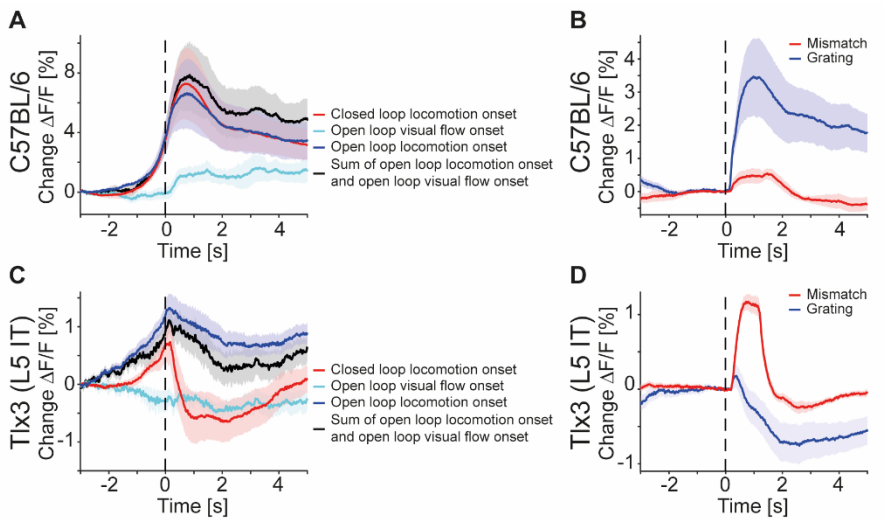

Figure S2. In V1, the sum of locomotion and visual flow onset could not explain the closed loop locomotion onset response of L5 IT neurons. Related to Figure 1.

(**A**) Average responses during closed (red) and open loop (blue) locomotion onsets, as well as open loop visual flow (turquoise) onsets, and the sum of open loop locomotion and open loop visual flow onsets (black) in C57BL/6 mice that expressed GCaMP brain wide (6 mice). Closed loop locomotion onset responses in V1 were larger than open loop locomotion onset responses, and part of this difference could be explained by the visual flow onset responses. Shading indicates SEM over mice.

(**B**) Average response during mismatch (red) and full-field drifting grating onsets (blue) in 6 C57BL/6 mice that expressed GCaMP brain wide. Same data as in **Figures 3B and 3C**. Shading indicates SEM over mice.

(**C**) As in **A**, but for Tlx3-Cre x Ai148 mice that expressed GCaMP6 in L5 IT neurons (15 mice). Closed loop locomotion onset responses in V1 could not be explained as the sum of open loop locomotion and visual flow onset responses.

(**D**) As in **B**, but for Tlx3-Cre x Ai148 mice that expressed GCaMP6 in L5 IT neurons (15 mice). Same data as in **Figures 3E and 3F**.

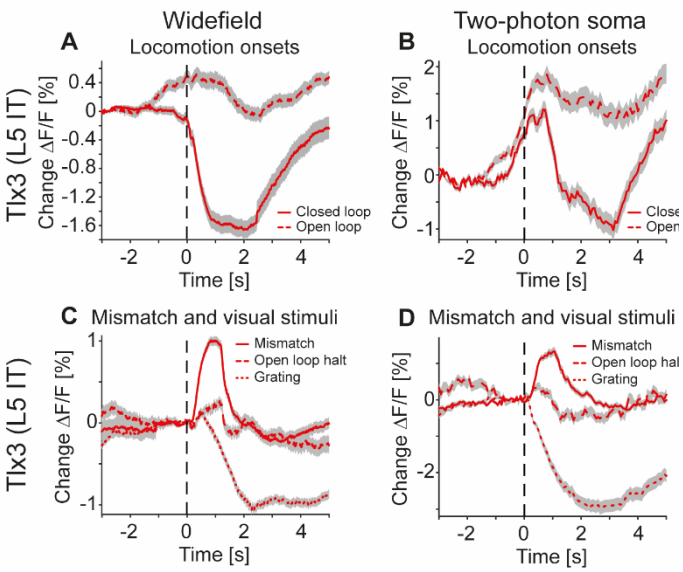

Figure S3. L5 IT soma recorded in V1 with two-photon imaging show similar patterns of activity as the widefield signal recorded at the surface of the dorsal cortex. Related to Figure 1.

(**A**) Average response of V1 recorded with the widefield macroscope during closed (solid, 1012 onsets) or open loop (dashed, 678 onsets) locomotion onsets in 7 Tlx3-Cre x Ai148 mice that expressed GCaMP6 in L5 IT neurons.

(**B**) Average response of L5 soma in V1, recorded with two-photon imaging in the same 7 Tlx3-Cre x Ai148 mice that expressed GCaMP6 in L5 IT neurons as in **A**, during either closed loop (solid) or open loop (dashed) locomotion onsets. Shading indicates SEM over 8434 neurons.

(**C**) As in **A**, but for responses to mismatches (solid, 1038 onsets), open loop halts (dashed, 410 onsets) or drifting grating onsets (dotted, 2014 onsets). Shading indicates SEM over onsets.

(**D**) As in **B**, but for responses to mismatches (solid), open loop halts (dashed) or drifting grating onsets (dotted). Shading indicates SEM over 8434 neurons.

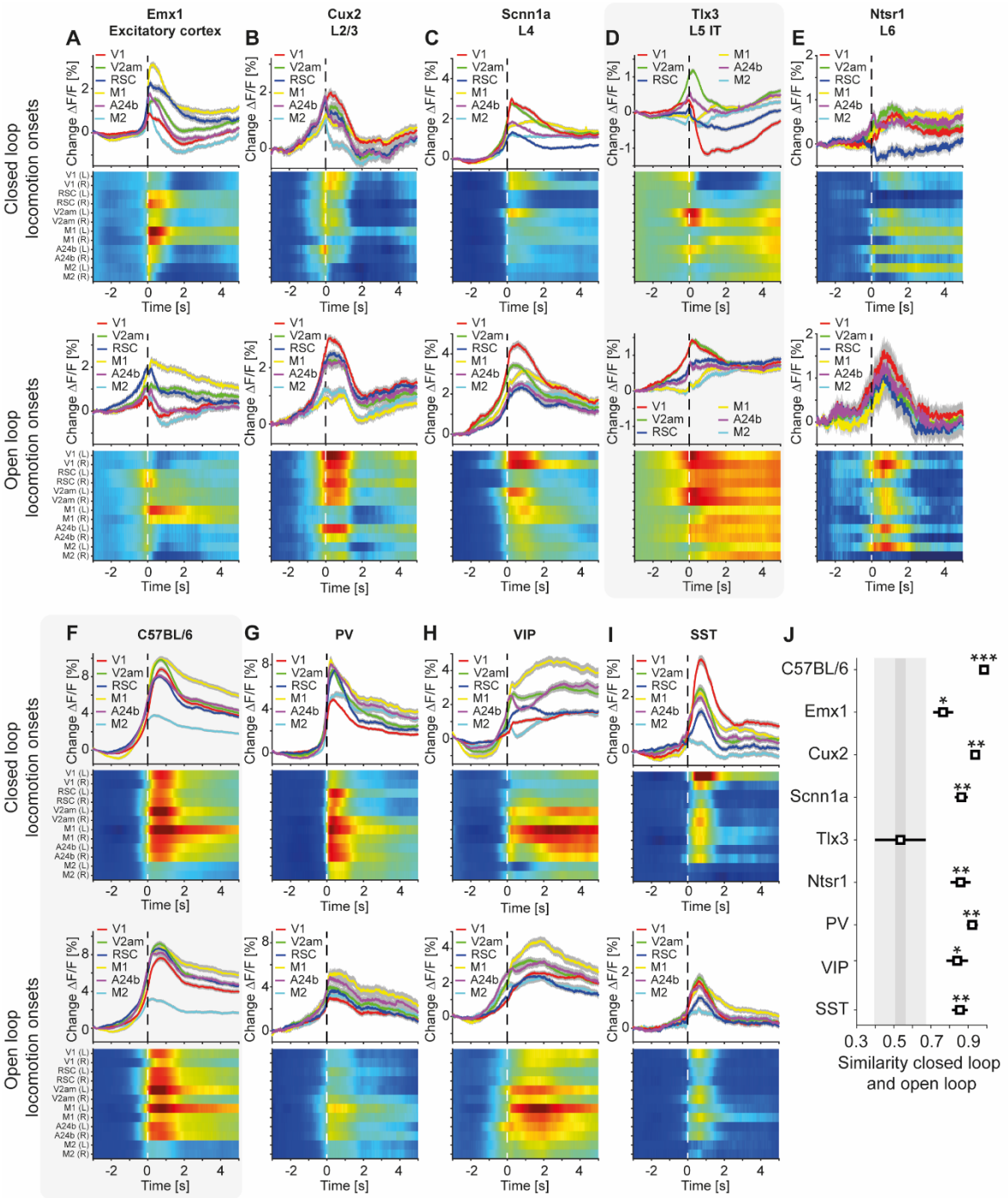

Figure S4. L5 IT neurons had strikingly different responses during closed and open loop locomotion onsets compared to other cortical neuron types. Related to Figure 1.

(**A**) Average response during closed loop locomotion onsets (top, 438 onsets) and open loop locomotion onsets (bottom, 286 onsets) in 4 Emx1-Cre mice that expressed GCaMP6 in excitatory cortical neurons. Shading indicates SEM over onsets. Heatmaps are scaled to the y-axis limits of the plot above (blue low, red high).

646 (**B**) As in **A**, but for 4 Cux2-CreERT2 x Ai148 mice that expressed GCaMP6 in upper layer excitatory
647 neurons (415 closed loop and 433 open loop locomotion onsets).

648 (**C**) As in **A**, but for 7 Scnn1a-Cre x Ai148 mice that expressed GCaMP6 in L4 excitatory neurons (839
649 closed loop and 313 open loop locomotion onsets).

650 (**D**) As in **A**, but for 15 Tlx3-Cre x Ai148 mice that expressed GCaMP6 specifically in L5 IT neurons
651 (1919 closed loop and 1125 open loop locomotion onsets). Data are the same as in **Figures 1I and**
652 **1K**.

653 (**E**) As in **A**, but for 3 Ntsr1-Cre x Ai148 mice that expressed GCaMP6 in excitatory L6 neurons (368
654 closed loop and 112 open loop locomotion onsets).

655 (**F**) As in **A**, but for 6 C57BL/6 mice that expressed GCaMP brain wide (907 closed loop and 598 open
656 loop locomotion onsets). Data are the same as in **Figures 1F and 1G**.

657 (**G**) As in **A**, but for 2 PV-Cre x Ai148 mice that expressed GCaMP6 in PV neurons (236 closed loop
658 and 110 open loop locomotion onsets).

659 (**H**) As in **A**, but for 6 VIP-Cre x Ai148 mice that expressed GCaMP6 in VIP neurons (618 closed loop
660 and 376 open loop locomotion onsets)

661 (**I**) As in **A**, but for 5 SST-Cre mice that expressed GCaMP6 in SST neurons (747 closed loop and 558
662 open loop locomotion onsets).

663 (**J**) Similarity of the average closed and open loop locomotion onset responses quantified as the
664 correlation coefficient between the two in a window -5 s to +3 s around locomotion onset (see
665 Methods). Error bars indicate SEM over mice that had an average locomotion onset response of at
666 least 1% $\Delta F/F$ in either the closed or the open loop condition (6 C57BL/6 mice, 4 Emx1-Cre mice, 7
667 Scnn1a-Cre mice, 14 Tlx3-Cre mice, 2 Ntsr1-Cre mice, 2 PV-Cre mice, 6 VIP-Cre mice, 6 Sst-Cre mice,
668 3 Cux2-CreERT2 mice). Statistical comparisons are against the Tlx3 data: n.s.: not significant, *: $p < 0.05$, **: $p < 0.01$, ***: $p < 0.001$. See **Table S1** for all information on statistical testing.

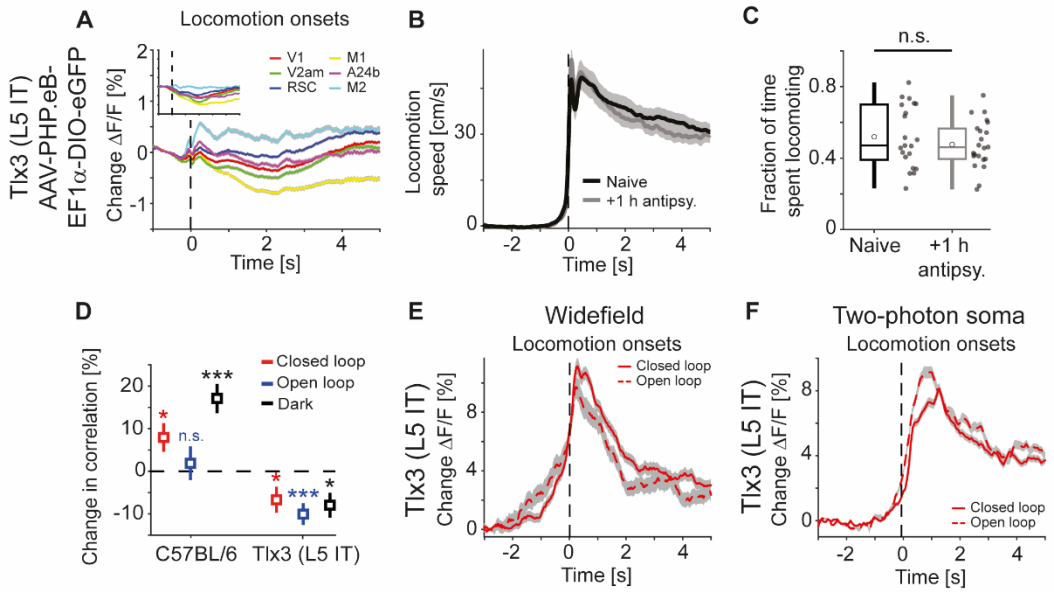

Figure S5. Additional information for antipsychotic drug data. Related to Figure 4.

(**A**) Average hemodynamic response during locomotion onsets in 7 Tlx3 mice that had been retro-orbitally injected with an AAV-PHP.eB-DIO-eGFP to express eGFP in L5 IT neurons (2331 onsets, responses were averaged across corresponding regions in both hemispheres) after a single injection of the antipsychotic drug clozapine (see Methods). Shading indicates SEM over onsets. Inset: Comparison of responses to locomotion onsets in the same mice before clozapine injection (same data as in **Figure S1C**, top panel).

(**B**) Average locomotion speed in 21 naive mice (black) and 22 mice that had been injected with either of the antipsychotic drugs clozapine, aripiprazole, or haloperidol (gray), for the data acquisition timepoint +1 h after injection. Shading indicates SEM over mice.

(**C**) Fraction of time spent locomoting above threshold (see Methods) for the 21 naive mice (black) and 22 mice that had been injected with either of the antipsychotic drugs clozapine, aripiprazole or haloperidol, for the data acquisition timepoint +1 h after injection (gray). Boxes represent the median and the interquartile range. The open circles indicate the mean of the distributions. The whiskers mark 1.5 times the interquartile range. Dots are the individual data points.

(**D**) Average correlation of activity and locomotion speed in dorsal cortex was increased after a single injection of the antipsychotic drug clozapine in 4 C57BL/6 mice that expressed GCaMP brain wide but decreased in 5 Tlx3-Cre x Ai148 mice that expressed GCaMP6 in L5 IT neurons, for all types of visual feedback. Error bars indicate SEM over mice and corresponding dorsal cortex regions (see Methods). n.s.: not significant, *: $p < 0.05$, ***: $p < 0.001$. See **Table S1** for all information on statistical testing.

(**E**) Average response of V1 recorded with the widefield macroscope during locomotion onsets in closed loop (solid, 376 onsets) or open loop (dashed, 245 onsets) in 3 Tlx3-Cre x Ai148 mice that expressed GCaMP6 in L5 IT neurons and that had received an injection of the antipsychotic drug clozapine. Shading indicates SEM over onsets.

(**F**) As in **E**, for the same 3 Tlx3 x Ai148 mice, but for responses recorded at L5 IT soma with two-photon imaging. Shading indicates SEM over 5595 neurons.

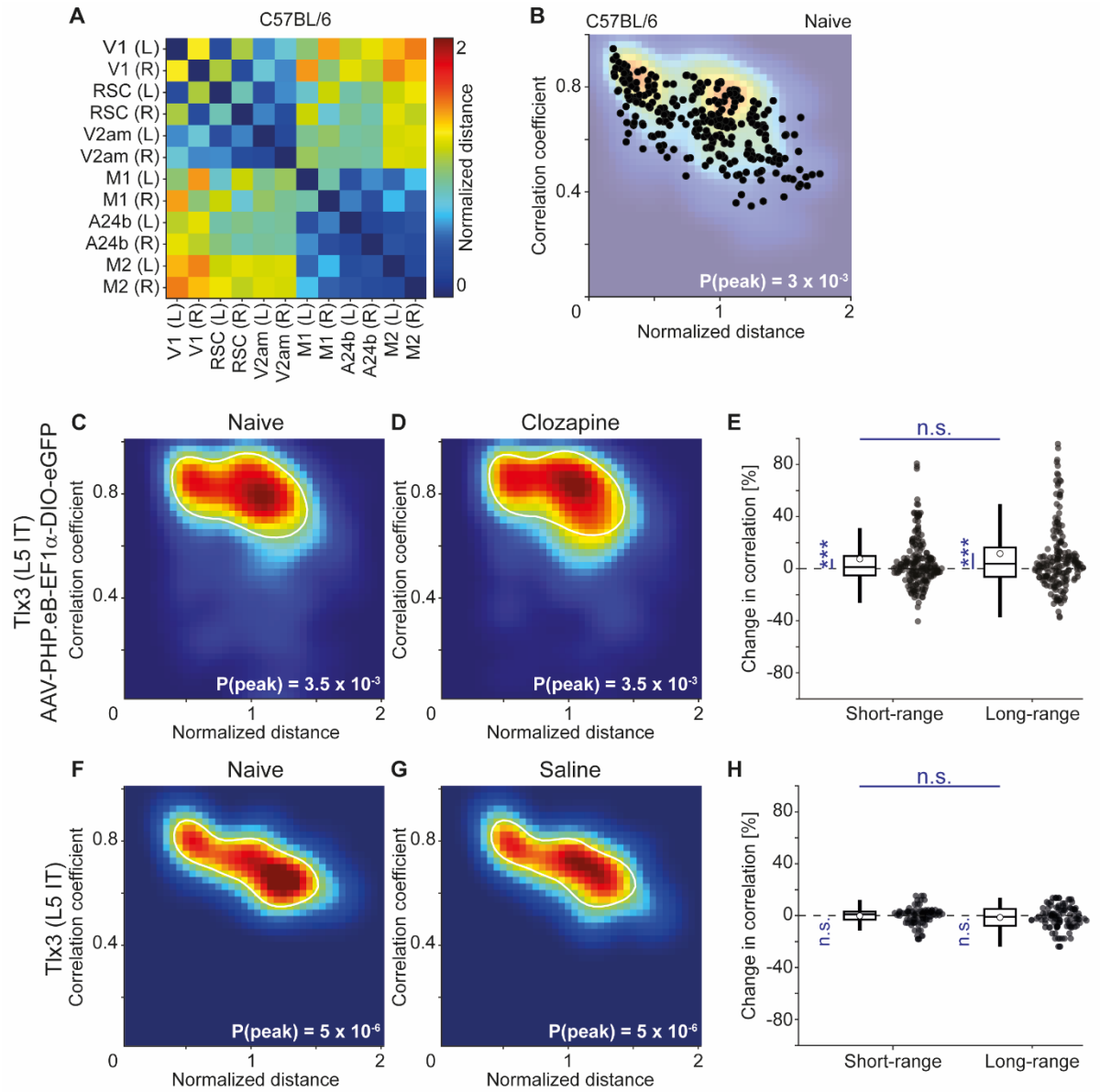

Figure S6. Calculation of the distance-correlation heatmaps. Related to Figure 5.

(**A**) For each pair of dorsal cortex regions, we calculated the distance between the regions in a top-down view of dorsal cortex, normalized by the distance between bregma and lambda for each mouse (data are from an example C57BL/6 mouse that expressed GCaMP6 brain wide).

(**B**) For each pair, we then plotted the activity correlation against this distance as calculated in **A** (black dots). We then interpolated this distribution using a 40-by-40 2D grid to obtain the density plots (faded background), shown for all mice and pairs in **Figures 6, 7, and S6-S8**.

(**C**) Density map of correlation coefficients as a function of distance between the regions, normalized across mice by the bregma-lambda distance (see panel **B** and Methods), for 6 Tlx3-Cre mice that had been retro-orbitally injected with an AAV-PHP.eB-DIO-eGFP to express eGFP in L5 IT neurons. Peak density is indicated at the bottom right of the plot and corresponds to the maximum value of the color scale (dark red). The white line is a contour line drawn at 50% of peak value.

(**D**) As in **C**, but for the same 6 Tlx3-Cre mice that expressed eGFP in L5 IT neurons after a single injection of the antipsychotic drug clozapine. The white line is the contour from panel **C** for comparison.

(**E**) Clozapine induced change in the fluorescence correlation between regions, normalized to the correlation coefficient in the naive state, in 6 Tlx3-Cre mice that expressed eGFP in L5 IT neurons. Data were split into short- and long-range activity correlations (see Methods). Boxes represent the median and the interquartile range. The open circle indicates the mean of the distribution. The whiskers mark 1.5 times the interquartile range. Dots are the individual data points (short-range: 204 pairs, long-range: 192 pairs). ***: $p < 0.001$, n.s.: not significant. See **Table S1** for all information on statistical testing.

(**F**) As in **C**, but for 3 Tlx3-Cre x Ai148 mice that expressed GCaMP6 in L5 IT neurons.

(**G**) As in **F**, but after a single injection of saline. The white line is the contour line from panel **F** for comparison.

(**H**) Saline induced change in the activity correlation between regions, normalized to the correlation coefficient in the naive state, in 3 Tlx3-Cre x Ai148 mice. Data were split into short- and long-range activity correlations (see Methods). Boxes represent the median and the interquartile range. The open circle indicates the mean of the distribution. The whiskers mark 1.5 times the interquartile range. Dots are the individual data points (short-range: 93 pairs, long-range: 105 pairs). n.s.: not significant. See **Table S1** for all information on statistical testing.

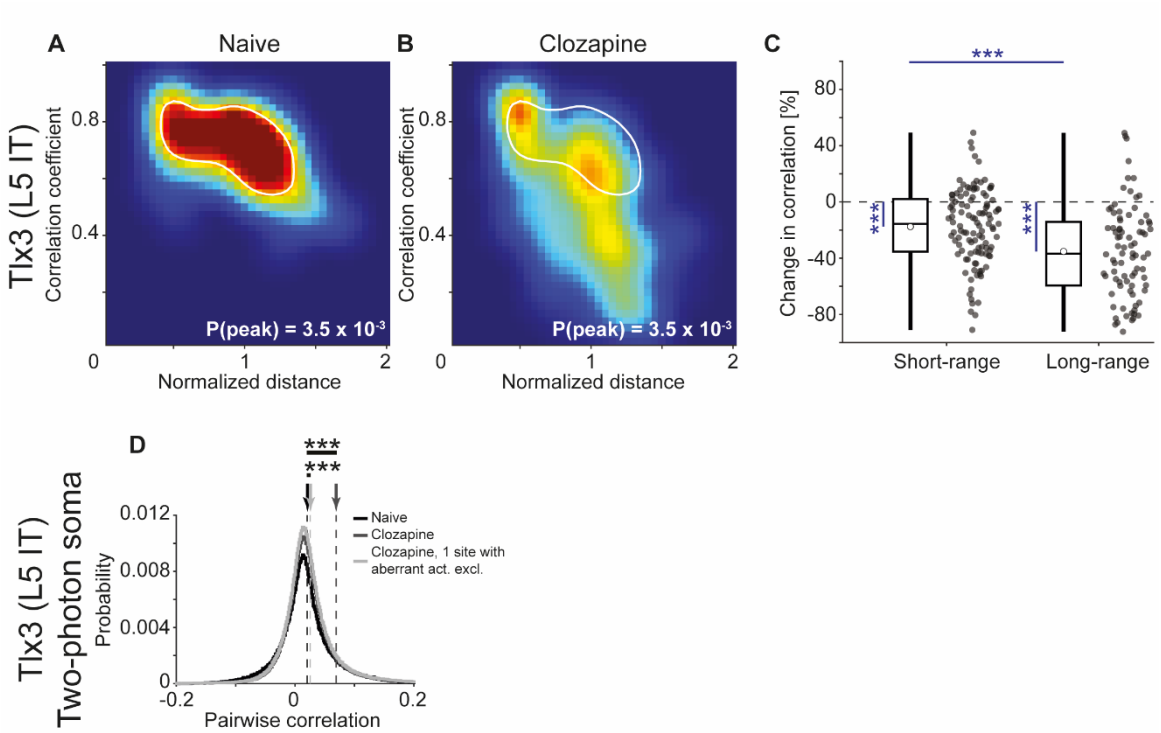

730

731 **Figure S7. The clozapine induced decorrelation was not present in local somatic correlations.**
732 **Related to Figure 6.**

733 (**A**) Density map of correlation coefficients as a function of distance between the regions, normalized
734 across mice by the bregma-lambda distance (see **Figures S6A and S6B**, and Methods), for 3 Tlx3-Cre
735 x Ai148 mice that expressed GCaMP6 in L5 IT neurons. Peak density is indicated at the bottom right
736 of the plot and corresponds to the maximum value of the color scale (dark red). The white line is a
737 contour line drawn at 50% of peak value.

738 (**B**) As in **A**, but for the same 3 Tlx3-Cre x Ai148 mice after a single injection of the antipsychotic drug
739 clozapine. The white line is the contour line from panel **A** for comparison.

740 (**C**) Clozapine induced change in the activity correlation between regions, normalized to the
741 correlation coefficient in the naive state, in 3 Tlx3-Cre x Ai148 mice. Data were split into short- and
742 long-range activity correlations (see Methods). Boxes represent the median and the interquartile
743 range. The open circle indicates the mean of the distribution. The whiskers mark 1.5 times the
744 interquartile range. Dots are the individual data points (short-range: 114 pairs, long-range: 84 pairs).
745 ***, $p < 0.001$. See **Table S1** for all information on statistical testing.

746 (**D**) Distribution of pairwise neuronal activity correlations recorded with two-photon imaging at the
747 L5 soma, in the same 3 Tlx3-Cre x Ai148 mice as in panels **A-C**, before (naive, black, 1991 neurons
748 and 384108 pairs) and after injection of the antipsychotic drug clozapine (dark gray, 7863 neurons
749 and 885596 pairs or pale gray, 1 field of view excluded, 7534 neurons and 831640 pairs). Dashed
750 lines mark the mean of the respective distributions as indicated by the arrows on top. Note that
751 after clozapine injection, we observed aberrantly high neuronal synchrony in 1 out of 25 recorded
752 fields of view that substantially increased the average pairwise correlation as indicated by the two

753 curves that compare the clozapine data. In either comparison, clozapine significantly increased local
754 pairwise activity correlations.

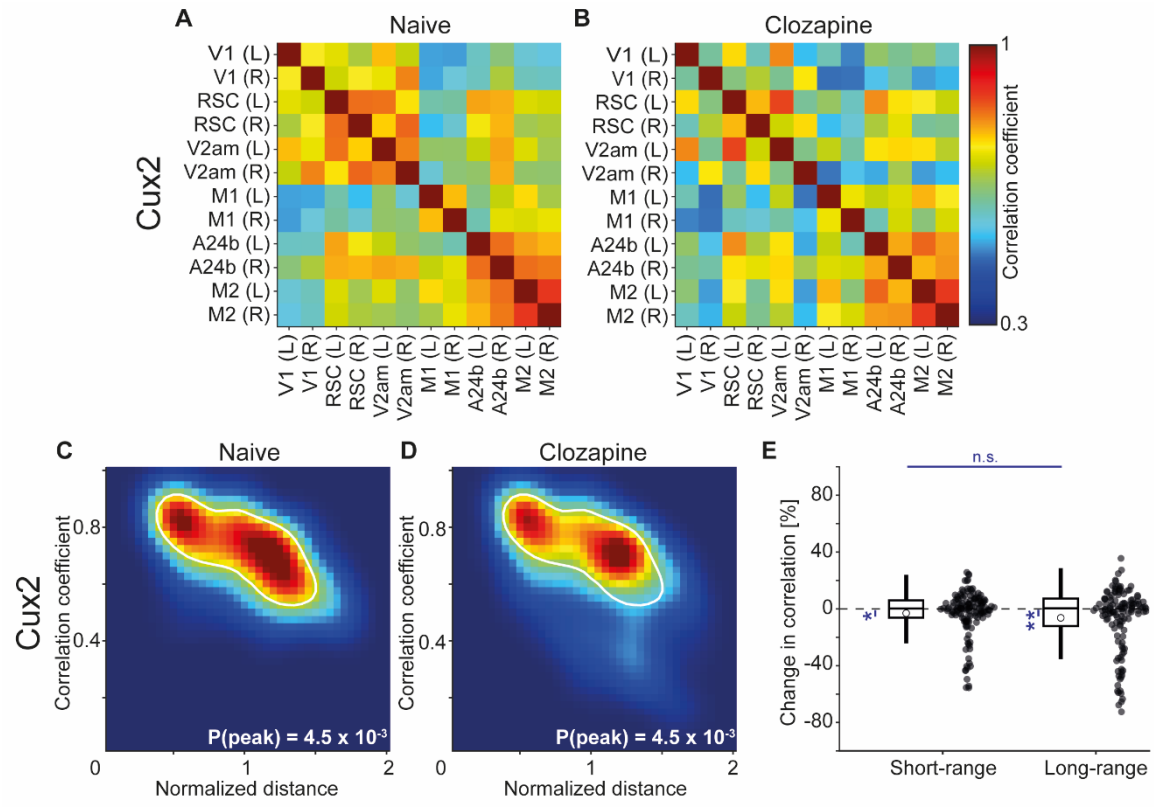

Figure S8. The clozapine induced decorrelation of dorsal cortex activity was weaker in superficial cortical layers than in L5. Related to Figure 6.

(**A**) Average correlation of activity between the 12 regions of interest in 4 Cux2-CreERT2 x Ai148 mice that expressed GCaMP6 in upper layer excitatory neurons.

(**B**) As in **A**, but for the same 4 Cux2-CreERT2 x Ai148 mice after a single injection of the antipsychotic drug clozapine.

(**C**) Density map of correlation coefficients as a function of distance between the regions, normalized across mice by the bregma-lambda distance (see **Figure S6A and S6B**, and Methods), for 4 naive Cux2-CreERT2 x Ai148 mice that expressed GCaMP6 in upper layer excitatory neurons. Peak density is indicated at the bottom right of the plot and corresponds to the maximum value of the color scale (dark red). The white line is a contour line drawn at 50% of peak value.

(**D**) As in **C**, but for the same 4 Cux2-CreERT2 x Ai148 mice after a single injection of the antipsychotic drug clozapine. The white line is the contour line from panel **C** for comparison.

(**E**) Clozapine induced change in the activity correlation between regions, normalized to the correlation coefficient in the naive state, in 4 Cux2-CreERT2 x Ai148 mice. Data were split into short- and long-range activity correlations (see Methods). Boxes represent the median and the interquartile range. The open circle indicates the mean of the distribution. The whiskers mark 1.5 times the interquartile range. Dots are the individual data points (short-range: 137 pairs, long-range: 127 pairs). n.s.: not significant, *: $p < 0.05$, **: $p < 0.01$. See **Table S1** for all information on statistical testing.

SUPPLEMENTAL TABLES

Table S1. Statistical comparisons for bar and violin plots.

Figure reference	Description (N_1 vs N_2)	Test	N_1 (mice)	N_2 (mice)	Unit	P-value
Figure 1L	Tlx3 vs C57BL/6	Bootstrap	12 (15)	12 (6)	Regions	$<10^{-4}$
	Tlx3 vs Emx1	Bootstrap	12 (15)	12 (4)	Regions	0.00135
	Tlx3 vs Cux2	Bootstrap	12 (15)	12 (4)	Regions	$<10^{-4}$
	Tlx3 vs Scnn1a	Bootstrap	12 (15)	12 (7)	Regions	$<10^{-4}$
	Tlx3 vs Ntsr1	Bootstrap	12 (15)	12 (3)	Regions	0.4541
	Tlx3 vs PV	Bootstrap	12 (15)	12 (2)	Regions	$<10^{-4}$
	Tlx3 vs VIP	Bootstrap	12 (15)	12 (6)	Regions	0.0001
	Tlx3 vs SST	Bootstrap	12 (15)	12 (5)	Regions	0.0131
	ANOVA	ANOVA	108 (54)	N/A	Regions	$< 10^{-5}$
Figure 2B	V1					
	Closed loop vs open loop	Hierachical bootsstrap	308 (6)	316 (6)	Sessions	0.9856
	Closed loop vs dark	Hierachical bootsstrap	308 (6)	68 (6)	Sessions	0.9631
	Open loop vs dark	Hierachical bootsstrap	316 (6)	68 (6)	Sessions	0.8968
	RSC					
	Closed loop vs open loop	Hierachical bootsstrap	308 (6)	316 (6)	Sessions	0.3423
	Closed loop vs dark	Hierachical bootsstrap	308 (6)	68 (6)	Sessions	0.1492
	Open loop vs dark	Hierachical bootsstrap	316 (6)	68 (6)	Sessions	0.2362
	V2am					
	Closed loop vs open loop	Hierachical bootsstrap	308 (6)	316 (6)	Sessions	0.4576
	Closed loop vs dark	Hierachical bootsstrap	308 (6)	68 (6)	Sessions	0.4694
	Open loop vs dark	Hierachical bootsstrap	316 (6)	68 (6)	Sessions	0.4961
	M1					
	Closed loop vs open loop	Hierachical bootsstrap	308 (6)	316 (6)	Sessions	0.4417
	Closed loop vs dark	Hierachical bootsstrap	308 (6)	68 (6)	Sessions	0.06
	Open loop vs dark	Hierachical bootsstrap	316 (6)	68 (6)	Sessions	0.0788
	A24b					
	Closed loop vs open loop	Hierachical bootsstrap	308 (6)	316 (6)	Sessions	0.8310
	Closed loop vs dark	Hierachical bootsstrap	308 (6)	68 (6)	Sessions	0.2194
	Open loop vs dark	Hierachical bootsstrap	316 (6)	68 (6)	Sessions	0.0846
	M2					
	Closed loop vs open loop	Hierachical bootsstrap	308 (6)	316 (6)	Sessions	0.4593
	Closed loop vs dark	Hierachical bootsstrap	308 (6)	68 (6)	Sessions	0.2373

	Open loop vs dark	Hierachical bootsstrap	316 (6)	68 (6)	Sessions	0.2674
Figure 2D	V1					
	Closed loop vs open loop	Hierachical bootsstrap	420 (15)	394 (15)	Sessions	$<10^{-4}$
	Closed loop vs dark	Hierachical bootsstrap	420 (15)	194 (15)	Sessions	$<10^{-4}$
	Open loop vs dark	Hierachical bootsstrap	394 (15)	194 (15)	Sessions	0.2103
	RSC					
	Closed loop vs open loop	Hierachical bootsstrap	420 (15)	394 (15)	Sessions	$<10^{-4}$
	Closed loop vs dark	Hierachical bootsstrap	420 (15)	194 (15)	Sessions	0.0001
	Open loop vs dark	Hierachical bootsstrap	394 (15)	194 (15)	Sessions	0.0021
	V2am					
	Closed loop vs open loop	Hierachical bootsstrap	420 (15)	394 (15)	Sessions	$<10^{-4}$
	Closed loop vs dark	Hierachical bootsstrap	420 (15)	194 (15)	Sessions	$<10^{-4}$
	Open loop vs dark	Hierachical bootsstrap	394 (15)	194 (15)	Sessions	0.1337
	M1					
	Closed loop vs open loop	Hierachical bootsstrap	420 (15)	394 (15)	Sessions	$<10^{-4}$
	Closed loop vs dark	Hierachical bootsstrap	420 (15)	194 (15)	Sessions	0.3115
	Open loop vs dark	Hierachical bootsstrap	394 (15)	194 (15)	Sessions	0.0002
	A24b					
	Closed loop vs open loop	Hierachical bootsstrap	420 (15)	394 (15)	Sessions	$<10^{-4}$
	Closed loop vs dark	Hierachical bootsstrap	420 (15)	194 (15)	Sessions	0.3511
	Open loop vs dark	Hierachical bootsstrap	394 (15)	194 (15)	Sessions	0.0001
	M2					
	Closed loop vs open loop	Hierachical bootsstrap	420 (15)	394 (15)	Sessions	0.0005
	Closed loop vs dark	Hierachical bootsstrap	420 (15)	194 (15)	Sessions	0.2686
	Open loop vs dark	Hierachical bootsstrap	394 (15)	194 (15)	Sessions	0.0156
Figure 6C	Short-range vs no change	T-test	122 (4)	-	Pairs	0.3791
	Long-range vs no change	T-test	142 (4)	-	Pairs	0.9035
	Short-range vs long-range	Ranksum	122 (4)	142 (4)	Pairs	0.0511
Figure 6F	Short-range vs no change	T-test	182 (5)	-	Pairs	$<10^{-5}$
	Long-range vs no change	T-test	148 (5)	-	Pairs	$<10^{-10}$
	Short-range vs long-range	Ranksum	182 (5)	148 (5)	Pairs	$<10^{-4}$
Figure 7C	Short-range vs no change	T-test	114 (3)	-	Pairs	$<10^{-5}$
	Long-range vs no change	T-test	84 (3)	-	Pairs	$<10^{-7}$
	Short-range vs long-range	Ranksum	114 (3)	84 (3)	Pairs	0.0347
Figure 7F	Short-range vs no change	T-test	114 (3)	-	Pairs	0.7058
	Long-range vs no change	T-test	84 (3)	-	Pairs	0.0435
	Short-range vs long-range	Ranksum	114 (3)	84 (3)	Pairs	0.0199
Figure 7I	Short-range vs no change	T-test	114 (3)	-	Pairs	0.4865
	Long-range vs no change	T-test	84 (3)	-	Pairs	0.2184

	Short-range vs long-range	Ranksum	114 (3)	84 (3)	Pairs	0.1633
Figure S4J	Tlx3 vs C57BL/6	Bootstrap	14	6	Mice	$<10^{-4}$
	Tlx3 vs Emx1	Bootstrap	14	4	Mice	0.0469
	Tlx3 vs Cux2	Bootstrap	14	3	Mice	0.0002
	Tlx3 vs Scnn1a	Bootstrap	14	7	Mice	0.0030
	Tlx3 vs Ntsr1	Bootstrap	14	2	Mice	0.0050
	Tlx3 vs PV	Bootstrap	14	2	Mice	0.0004
	Tlx3 vs VIP	Bootstrap	14	6	Mice	0.0125
	Tlx3 vs SST	Bootstrap	14	6	Mice	0.0073
	ANOVA	ANOVA	54	N/A	Mice	0.1172
Figure S5C	Naive vs +1 h antipsy.	Ranksum	21	22	Mice	0.4735
Figure S5D	C57BL/6					
	Closed loop vs no change	T-test	24 (4)	-	Regions	0.0277
	Open loop vs no change	T-test	24 (4)	-	Regions	0.6384
	Dark vs no change	T-test	24 (4)	-	Regions	$<10^{-4}$
	Tlx3					
	Closed loop vs no change	T-test	30 (5)	-	Regions	0.0365
	Open loop vs no change	T-test	30 (5)	-	Regions	0.0004
	Dark vs no change	T-test	30 (5)	-	Regions	0.0104
Figure S6E	Short-range vs no change	T-test	204 (7)	-	Pairs	0.0006
	Long-range vs no change	T-test	192 (7)	-	Pairs	$<10^{-4}$
	Short-range vs long-range	Ranksum	204 (7)	192 (7)	Pairs	0.2540
Figure S6H	Short-range vs no change	T-test	93 (3)	-	Pairs	0.7884
	Long-range vs no change	T-test	105 (3)	-	Pairs	0.1176
	Short-range vs long-range	Rank-sum	93 (3)	105 (3)	Pairs	0.2319
Figure S7C	Short-range vs no change	T-test	114 (3)	-	Pairs	$<10^{-4}$
	Long-range vs no change	T-test	84 (3)	-	Pairs	$<10^{-4}$
	Short-range vs long-range	Ranksum	114 (3)	84 (3)	Pairs	$<10^{-4}$
Figure S7D	Naive vs clozapine	Ranksum	384108 (7)	885596	Pairs	$<10^{-4}$
	Naive vs clozapine 1 site excl.	Ranksum	384108 (7)	831640	Pairs	$<10^{-4}$
Figure S8E	Short-range vs no change	T-test	137 (4)	-	Pairs	0.0262
	Long-range vs no change	T-test	127 (4)	-	Pairs	0.0019
	Short-range vs long-range	Ranksum	137 (4)	127 (4)	Pairs	0.9537

780 **Table S2. Indicator expression strategy in individual mice.**

Nbr. mice	Genotype	Virus	Figures
3	C57BL/6	AAV-PHP.eB-hSyn1-jGCaMP7f	**1C, 1F-1H, 1L, 2A and 2B, 3A-3C, 4A-4C, 5A and 5B, 6A-6C, S2, S4F, S4J, S5B-S5D, S6A and S6B**
3	C57BL/6	AAV-PHP.eB-EF1α-GCaMP6s	**1F-1H, 1L, 2B, 3B and 3C, 4A-4C, 5A and 5B, 6A-6C, S2, S4F, S4J, S5B-S5D**
8	C57BL/6	AAV-PHP.eB-EF1α-eGFP	**S1**
4	Emx1-Cre	AAV-PHP.eB-DIO-EF1α-GCaMP6s	**1L, S4A and S4J**
4	Cux2-CreERT2 x Ai148	-	**1L, S4B, S4J and S8**
7	Scnn1a-Cre x Ai148	-	**1L, S4C and S4J**
25	Tlx3-Cre x Ai148	-	**1D, 1I-1L, 2C and 2D, 3D-3F, 4D-4F, 5C and 5D, 6D-6F, 7, 8, S2, S3D, S4D, S4J, S5B-S5F, S6G-S6H, S7**
7	Tlx3-Cre	AAV-PHP.eB-EF1α-DIO-eGFP	**S1C and S1D, S5A, S6C-S6E**
3	Ntsr1-Cre x Ai148	-	**1L, S4E and S4J**
2	PV-Cre x Ai148	-	**1L, S4G and S4J**
6	VIP-Cre x Ai148	-	**1L, S4H and S4J**
4	SST-Cre	AAV-PHP.eB-DIO-EF1α-jGCaMP7f	**1L, S4I and S4J**
1	SST-Cre x Ai148	-	**1L, S4I and S4J**

781

782 **METHODS**

783 **Key Resource Table**

REAGENT or RESOURCE	Source	Identifier
Bacterial and virus strains		
AAV-PHP.eB-hSyn1-jGCaMP7f (10^{13} GC/ml)	FMI vector core	vector.fmi.ch
AAV-PHP.eB-EF1α-GCaMP6s (10^{13} GC/ml)	FMI vector core	vector.fmi.ch
AAV-PHP.eB-DIO-EF1α-GCaMP6s (10^{13} GC/ml)	FMI vector core	vector.fmi.ch
AAV-PHP.eB-DIO-EF1α-jGCaMP7f (10^{12} GC/ml)	FMI vector core	vector.fmi.ch
AAV-PHP.eB-EF1α-eGFP (10^{13} GC/ml)	FMI vector core	vector.fmi.ch
AAV-PHP.eB-EF1α-DIO-eGFP (10^{15} GC/ml)	FMI vector core	vector.fmi.ch
Chemicals, peptides, and recombinant proteins		
Fentanyl citrate	Actavis	CAS 990-73-8
Midazolam (Dormicum)	Roche	CAS 59467-96-8
Medetomidine (Domitor)	Orion Pharma	CAS 86347-14-0
Ropivacaine	Presenius Kabi	CAS 132112-35-7
Lidocaine	Bichsel	CAS 137-58-6
Buprenorphine	Reckitt Benckiser Healthcare	CAS 52485-79-7
Ophthalmic gel (Humigel)	Virbac	N/A
Flumazenil (Anexate)	Roche	CAS 78755-81-4
Atipamezole (Antisedan)	Orion Pharma	CAS 104054-27-5
N-Butyl-2-cyanoacrylate (Histoacryl)	Braun	CAS 6606-65-1
Dental cement (Paladur)	Heraeus Kulzer	CAS 9066-86-8
Metacam	Boehringer Ingelheim	CAS 71125-39-8
Clozapine (powder)	Novartis	CAS 5786-21-0
Aripiprazole (intramuscular injection solution 7.5 mg/ml)	Otsuka Pharmaceutical	CAS 129722-12-9
Haloperidol (intramuscular injection solution 5 mg/ml)	Janssen	CAS 52-86-8
Amphetamine (powder)	Hänseler	CAS 60-13-9
Tamoxifen food	Envigo	CAS 10540-29-1 (TD.55125)
Deposited data		
All data and code used to generate manuscript figures	This paper	data.fmi.ch
Experimental models: Organisms/strains		
Mus musculus: C57BL/6	Charles River	N/A
Mus musculus: Emx1$^{tm1(cre)Krj}$	Jackson Laboratories	RRID:IMSR_JAX:005628
Mus musculus: B6(Cg)-Cux2$^{tm3.1(cre/ERT2)Mull}$/Mmmh	MMRRC	RRID:MMRRC_032779-MU
Mus musculus: Scnn1a-cre3Aibs/J	Jackson Laboratories	RRID:IMSR_JAX:009613
Mus musculus: Tg(Tlx3-cre)PL56Gsat/Mmucd	MMRRC	RRID:MMRRC_041158-UCD
Mus musculus: Ntsr1$^{GN220Gsat/Mmucd}$	MMRRC	RRID:MMRRC_017266-UCD
Mus musculus: Pvalb$^{tm1(cre)Arbr}$	Jackson Laboratories	RRID:IMSR_JAX:008069
Mus musculus: Vip$^{tm1(cre)Zjh}$	Jackson Laboratories	RRID:IMSR_JAX:010908
Mus musculus: Sst$^{tm2.1(cre)Zjh}$	Jackson Laboratories	RRID:IMSR_JAX:018973
Mus musculus: Igs7$^{tm148.1(tetO-GCaMP6f,CAG-tTA2)Hze}$/J	Jackson Laboratories	RRID:IMSR_JAX:030328
Software and algorithms		
MATLAB (2021a)	The MathWorks	RRID:SCR_001622
LabVIEW	National Instruments	RRID:SCR_014325
Python	python.org	RRID:SCR_008394
Panda3D	panda3d.org	N/A

784

785 **Mice.** All animal procedures were approved by and carried out in accordance with guidelines of the
786 Veterinary Department of the Canton Basel-Stadt, Switzerland. The mice used for cell-type specfic
787 targeting and subsequent widefield imaging in this study were kept on a C57BL/6 background and
788 were of the following genotype: 6 C57BL/6 (Charles River Laboratories), 4 Emx1-Cre to target
789 expression to cortical excitatory neurons (Gorski et al., 2002), 4 Cux2-CreERT2 to target expression
790 to L2/3 and L4 excitatory neurons (Franco et al., 2012), 7 Scnn1a-Cre to target expression to a subset
791 of L4 excitatory neurons (Madisen et al., 2010), 25 Tlx3-Cre to target expression to a subset of L5 IT
792 neurons (Gerfen et al., 2013), 3 Ntsr1-Cre to target expression to a subset of L6 excitatory neurons
793 (Gong et al., 2007), and, to target inhibitory subpopulations, we used 2 PV-Cre (Hippenmeyer et al.,
794 2005), 6 VIP-Cre (Taniguchi et al., 2011), and 5 SST-Cre (Taniguchi et al., 2011) mice. Ai148 ((Daigle et
795 al., 2018), Jackson Laboratories, stock #030328) mice were used as breeders to drive GCaMP6f
796 expression in Cre positive neurons. An additional 8 C57BL/6 and 7 Tlx3-Cre mice were used in
797 experiments controlling for hemodynamic responses. To induce expression of Cre in the Cux2-
798 CreERT2 line, mice were provided for at least 1 week with tamoxifen containing food (Envigo, 400
799 mg tamoxifen per kg of food) as their sole food source. Mice were group housed in a vivarium
800 (light/dark cycle: 12/12 hours). Experimental mice were of either sex.

801 **Surgery and virus injections.** For all surgical procedures, mice were anesthetized using a mixture of
802 fentanyl (0.05 mg/kg; Actavis), midazolam (5.0 mg/kg; Dormicum, Roche), and medetomidine (0.5
803 mg/kg; Domitor, Orion). In a subset of mice (6 C57BL/6, 4 Emx1-Cre, and 4 SST-Cre mice), we
804 injected an AAV vector based on the PHP.eB capsid (Chan et al., 2017) retro-orbitally (6 μl each eye
805 of at least 10^{13} GC/ml) to drive expression of GCaMP under either the EF1α or hSyn1 promoter pan-
806 neuronally, or in a cell type specific manner using a double-floxed inverted open reading frame (DIO)
807 construct. For hemodynamic response control experiments, we used an AAV-PHP.eB-EF1α-eGFP to
808 pan-neuronally express eGFP (**Figures S1A and S1B)** or an AAV-PHP.eB-EF1α-DIO-eGFP to restrict
809 eGFP expression to L5 IT neurons in Tlx3-Cre mice (**Figures S1C and S1D, S5A, S6C-S6E**). To improve
810 optical access to the cortex, we implanted crystal skull cranial windows (Kim et al., 2016). Prior to
811 removing the skull plate overlying dorsal cortex, we recorded the location of bregma relative to
812 other landmarks on the skull. Superglue (Pattex) was used to glue the crystal skull in place in the
813 craniotomy. In a subset of mice, for the comparison of hemodynamic responses (**Figure S1A and**
814 **S1B**), we used a clear skull preparation (Guo et al., 2014). To do this, we attached the crystal skull
815 coverslip directly onto the cleaned skull surface with a three-component polymer (C&B Metabond,
816 Parkell). A custom-machined titanium head bar was attached to the skull using dental cement
817 (Paladur, Heraeus). An epifluorescence overview image was taken to mark reference points on the

818 dorsal cortical surface. Anesthesia was antagonized by an intraperitoneal injection of a mixture of
819 flumazenil (0.5 mg/kg; Anexate, Roche) and atipamezole (2.5 mg/kg; Antisedan, Orion Pharma). For
820 peri- and post-operative analgesia we injected buprenorphine (0.1 mg/kg; Reckitt Benckiser
821 Healthcare (UK) Ltd.) and Metacam (5 mg/kg; Boehringer Ingelheim). Imaging commenced at the
822 earliest 1 week after head bar implantation or 3 weeks after retro-orbital AAV injection. Clozapine
823 (Novartis), aripiprazole (Otsuka Pharmaceutical), haloperidol (Janssen), amphetamine (Hänseler), or
824 saline (0.9% NaCl in H_2O) was intraperitoneally injected at 0.2 μg/g - 10 μg/g, 0.2 μg/g, 0.1 μg/g, 4
825 μg/g body weight, or undiluted, respectively.

826 **Virtual reality setup and stimulus design.** For all experiments we used a virtual reality setup as
827 previously described (Leinweber et al., 2014). Mice were head-fixed and free to run on a spherical,
828 air-supported Styrofoam ball. A virtual corridor was projected (using a Samsung SP-F10M projector)
829 onto a toroidal screen positioned in front of the mouse covering a field of view of approximately 240
830 degrees horizontally and 100 degrees vertically. Recordings were blocked into 5-minute sessions.
831 Experiments typically commenced with 4 sessions of a closed loop condition in which the rotation of
832 the spherical treadmill was coupled to the movement in a virtual corridor. To introduce mismatches,
833 we broke the coupling between locomotion and visual flow by briefly halting visual flow for 1 s at
834 random times. Closed loop sessions were followed by 4 sessions of an open loop condition, in which
835 rotation of the spherical treadmill and movement in the virtual corridor were decoupled. The visual
836 stimulus consisted of a replay of the visual flow recorded in the previous closed loop condition.
837 Following this we recorded 2 sessions of what we refer to as a dark condition in which the virtual
838 reality was switched off. Please note, this was not complete darkness, primarily because the
839 shielding of the blue excitation light was not light proof. Finally, we recorded activity in 2 sessions of
840 a grating condition in which we presented drifting grating stimuli covering the full toroidal screen
841 placed in front of the mouse (8 directions of 6 s ± 2 s (mean ± SD) duration each with an inter-grating
842 interval of 4.5 s ± 1.5 s (mean ± SD) gray screen, presented in randomized order). These sessions,
843 totaling approximately 1 hour of recording time per day, were acquired for 3 consecutive days. For
844 mice in which we went on to test the effect of drugs on dorsal cortex activity, the first post-drug
845 injection data were acquired +1 h after drug injection (+30 mins in the case of amphetamine because
846 of faster onset kinetics of the drug) and further data were collected at the +24 h and +48 h
847 timepoints. Data in the manuscript are shown as the combined data over either all data collected
848 before drug injection (labelled as naive) or after substance injection (labelled as clozapine,
849 aripiprazole, haloperidol, amphetamine, or saline, respectively).

850 **Data acquisition.** All widefield imaging experiments were performed on a custom-built macroscope
851 consisting of commercially available objectives mounted face-to-face (Nikon 85 mm/f1.8 sample
852 side, Nikon 50 mm/f1.4 sensor side). We used a 470 nm LED (Thorlabs) powered by a custom-built
853 LED driver for exciting GCaMP (or eGFP) fluorescence through an excitation filter (SP490, Thorlabs)
854 reflected off a dichroic mirror (LP490, Thorlabs) placed in the parfocal plane of the objectives. Green
855 fluorescence was collected through a 525/50 emission filter on an sCMOS camera (PCO edge 4.2).
856 Apertures on objectives were usually kept maximally open and the current at the LED driver was
857 used to adjust fluorescence intensity to a value that was kept below 25% of the maximum dynamic
858 range of the sensor. In cases where this was not possible (e.g., transfection of eGFP yielded
859 extremely bright fluorescence, often visible with the naked eye), objective apertures were gradually
860 reduced to avoid overexposure of the sensor. LED illumination was adjusted with a collimator
861 (Thorlabs SM2F32-A) to achieve homogenous illumination across the surface of the cranial window.
862 The resulting Gaussian profile of the illumination cone was further trimmed with black tape on the
863 sample side objective to avoid light shining directly into the mouse's eye. An Arduino board (Arduino
864 Mega 2560) was used to control LED onsets synced to the frame trigger signal of the camera. The
865 duty cycle of the 470 nm LED was 90%. Raw images were acquired at full speed (100 Hz; except for
866 eGFP controls, which were acquired at 50 Hz effective frame rate) and full dynamic range (16 bit) of
867 the sensor. The raw images were cropped on-sensor and the resulting data was streamed to disk
868 with custom written software in LabVIEW (National Instruments), resulting in an effective pixel size
869 of 60 μm^2 at a standardized imaging resolution of 1108 pixels x 1220 pixels (1.35 MP).

870 Two-photon calcium imaging was performed using a custom-built microscope based on a Thorlabs B-
871 scope (Leinweber et al., 2014). Illumination source was a tunable femtosecond laser (Coherent
872 Chameleon) tuned to 930 nm. Emission light was band-pass filtered using a 525/50 filter for GCaMP
873 and detected using a GaAsP photomultiplier (H7422, Hamamatsu). Photomultiplier signals were
874 amplified (DHPCA-100, Femto), digitized (NI5772, National Instruments) at 800 MHz, and band-pass
875 filtered around 80 MHz using a digital Fourier-transform filter implemented in custom-written
876 software on an FPGA (NI5772, National Instruments). The scanning system of the microscope was
877 based on a 12 kHz resonant scanner (Cambridge Technology). Images were acquired at a resolution
878 of 750 pixels x 400 pixels at a 60 Hz frame rate and a piezo-electric linear actuator (P-726, Physik
879 Instrumente) was used to move the objective (Nikon 16x, 0.8 NA) in steps of 15 µm between frames
880 to acquire images at 4 different depths. This resulted in an effective frame rate of 15 Hz. The field of
881 view was 350 µm x 350 µm.

882 **Data processing.** Off-line data processing and data analysis (section below) were done with custom-
883 written MATLAB (2021a) scripts. For widefield macroscope imaging, raw movie data was manually
884 registered across days by aligning subsequent mean projections of the data to the first recorded
885 image sequence. We placed regions of interest (ROIs) relative to readily identifiable anatomical
886 landmarks that had been previously noted during cranial window surgery (see above). This resulted
887 in the selection of six 20 pixels x 20 pixels ROIs per hemisphere. Of those ROIs, we calculated the
888 activity as the $\Delta F/F_0$, wherein F_0 was the median fluorescence of the recording (approximately
889 30 000 frames in a 5 min recording). $\Delta F/F_0$ was corrected for slow fluorescence drift caused by
890 thermal brightening of the LED using 8th percentile filtering with a 62.5 s moving window similar to
891 what was described previously for two-photon imaging (Daniel A. Dombeck et al., 2007).

892 Raw two-photon imaging data were full-frame registered to correct for brain motion. Neurons were
893 manually selected based on mean and maximum fluorescence images. Raw fluorescence traces were
894 corrected for slow drift in fluorescence using an 8th percentile filtering with a 15 s window (Daniel A
895 Dombeck et al., 2007). $\Delta F/F$ traces were calculated as mean fluorescence in a selected region of
896 every imaging frame and subsequently subtracted and normalized by the median fluorescence.

897 **Data analysis.** Locomotion and visual flow onsets were determined based on threshold crossing of
898 locomotion or visual flow speed. To select only well isolated onsets, we used a speed threshold of 30
899 cm/s and excluded all onsets with locomotion or visual flow in the 3 s window preceding the onset.
900 To increase the number of locomotion onsets that passed the speed threshold criterion for the eGFP
901 imaging data (**Figures S1, S5A**), we excluded only those onsets if there was locomotion in the 1 s
902 window preceding onset.

903 All stimulus response curves (**Figures 1F-1L, 3B and 3C, 3E and 3F, 4, 8, S1-S4, S5A and S5B, S5E and**
904 **S5F**) were baseline subtracted. The baseline subtraction window for unpredictable stimuli
905 (mismatches and grating onsets) was -200 ms to 0 ms before stimulus onset. For closed loop and
906 open loop locomotion onsets, and open loop visual flow onsets, to accommodate calcium indicator
907 offset dynamics and potential anticipatory activity, we placed the baseline subtraction windows for
908 these onsets at -2900 ms to -2700 ms for GCaMP imaging, or -900 ms to -700 ms for eGFP imaging.
909 Varying this window within the bounds of offset dynamics of the indicator and anticipatory activity
910 onset did not change the conclusions drawn in this manuscript. Analyses in which image sequences
911 were aligned to event onsets (**Figures 1C-1D and 3**) used the same parameters as above.

912 On rare occasions, we observed seizure-like activity after antipsychotic drug injection. These events
913 resulted in atypically high levels of correlation, and to avoid them from influencing our conclusions

914 we excluded these data from further analysis. We excluded sessions if they contained an event in
915 which average activity of all 12 ROIs remained elevated above 30% $\Delta F/F$ for more than 10 s. This
916 criterion led to the exclusion of 0.26% of data (10 out of 3801 of 5 min recording sessions).

917 To quantify the similarity of closed loop and open loop locomotion onset responses shown in **Figure**
918 **1L** we calculated the correlation coefficient between the averaged responses (onsets and mice, 1 s
919 moving average) in a window -5 s to +3 s, for each ROI. For **Figure S4J**, we first averaged over onsets
920 and regions, which resulted in an average locomotion onset response curve for each mouse and
921 condition (closed and open loop). These curves were subsequently used for calculating the
922 correlation coefficient (per mouse) in the same window as above. For this analysis, we excluded
923 mice in which the responses were smaller than 1% $\Delta F/F$ in either of the two conditions (4 of 54
924 mice), as the correlation analysis yields noise in the absence of a clear response.

925 For the correlation analyses shown in **Figures 5-7, S6-S8**, we first calculated the correlation
926 coefficient of neuronal activity (or fluorescence change, in the case of Tlx3-Cre mice that had been
927 retro-orbitally injected with an AAV-PHP.eB-Ef1α-DIO-eGFP to express eGFP in L5 IT neurons) for all
928 possible pairs of the 12 regions of interest. We then determined the distance between each pair of
929 ROIs and normalized this value by the distance between bregma and lambda obtained from the
930 images during initial surgery for each mouse (**Figure S6A**). We plotted the correlation against the
931 distance for each pair of regions of interest and binned the data in a 40 x 40 grid and smoothed the
932 resulting image with a gaussian filter (**Figure S6B**), to obtain the heatmaps shown in **Figures 6A and**
933 **6B, 6D and 6E, 7A and 7B, 7D and 7E, 7G and 7H, S6B-S6D, S6G and S6H, S7A and S7B, S8C and S8D**.
934 Contour lines in the heatmaps were then drawn to 50% of the maximum value in the plot. The
935 boxplot quantifications (**Figures 6C, 6F, 7C, 7F, 7I, S6E, S6H, S7C, S8E**) were calculated as the change
936 in correlation coefficient of activity after and before treatment for all pairs of regions of interest,
937 normalized to the value before treatment and split into short- and long-range using a threshold of
938 0.9 of the bregma-lambda distance for each mouse. For pairwise neuronal correlations that had
939 been recorded with two-photon imaging (**Figure S7D**), we calculated the correlation coefficient
940 separately for all pairs of neurons within each field of view. We noticed extreme synchrony of
941 activity of L5 IT soma recorded in 1 field of view with two-photon imaging after clozapine injection
942 and show both distributions for all data as well as the distribution when this 1 field of view is
943 excluded.

944 For **Figure S2,** onset aligned data were first averaged for each mouse and then summed in the given
945 combinations. The SEM was calculated over mice.

To obtain the differences in the correlation between activity and locomotion after and before clozapine injection (**Figure S5D**), we first averaged all correlation coefficients in the individual sessions of a condition (closed loop, open loop, or dark) to generate one correlation coefficient per mouse and ROI, for each condition. We then calculated and plotted the difference between these correlation values after and before clozapine injection.

We used a hierarchical bootstrap (**Figures 2C and 2D**), or a bootstrap (where data were not nested, **Figure 1L and S4J**), distribution to estimate p-values. For hierarchical bootstrap, we first resampled the data (with replacement) at the level of mice, and then, from the selected mice, resampled for sessions. In cases where data were not nested, bootstrap samples were drawn from the distribution of data points. We then computed the mean of this bootstrap sample and repeated this 10 000 times to generate a bootstrap distribution of the mean estimate. The p-value was then defined as the proportion of bootstrap samples higher (or lower, depending on the hypothesis) than zero.

ACKNOWLEDGEMENTS

We thank Tingjia Lu for production of the AAV vectors, Rebecca Jordan for performing the clear skull implants used in the hemodynamic response measurements, and members of the Keller lab for discussion and support. This project has received funding from the Swiss National Science Foundation, the Novartis Research Foundation, and the European Research Council (ERC) under the European Union's Horizon 2020 research and innovation programme (grant agreement No 865617).

AUTHOR CONTRIBUTIONS

MH performed the experiments and analyzed the data. All authors wrote the manuscript.

CONFLICT OF INTEREST

Part of the results presented herein have been included in patent application EP22153051.1.

REFERENCES

Allen, W.E., Kauvar, I.V., Chen, M.Z., Richman, E.B., Yang, S.J., Chan, K., Gradinaru, V., Deverman, B.E., Luo, L., Deisseroth, K., 2017. Global Representations of Goal-Directed Behavior in Distinct Cell Types of Mouse Neocortex. Neuron 94, 891-907.e6. https://doi.org/10.1016/j.neuron.2017.04.017

Anderson, C.T., Sheets, P.L., Kiritani, T., Shepherd, G.M.G., 2010. Sublayer-specific microcircuits of corticospinal and corticostriatal neurons in motor cortex. Nat Neurosci 13, 739–744. https://doi.org/10.1038/nn.2538

Anticevic, A., Hu, X., Xiao, Y., Hu, J., Li, F., Bi, F., Cole, M.W., Savic, A., Yang, G.J., Repovs, G., Murray, J.D., Wang, X.-J., Huang, X., Lui, S., Krystal, J.H., Gong, Q., 2015. Early-course unmedicated schizophrenia patients exhibit elevated prefrontal connectivity associated with longitudinal change. J Neurosci 35, 267–286. https://doi.org/10.1523/JNEUROSCI.2310-14.2015

Aravanis, A.M., Wang, L.-P., Zhang, F., Meltzer, L.A., Mogri, M.Z., Schneider, M.B., Deisseroth, K., 2007. An optical neural interface: in vivo control of rodent motor cortex with integrated fiberoptic and optogenetic technology. J Neural Eng 4, S143-156. https://doi.org/10.1088/1741-2560/4/3/S02

Attinger, A., Wang, B., Keller, G.B., 2017. Visuomotor Coupling Shapes the Functional Development of Mouse Visual Cortex. Cell 169, 1291-1302.e14. https://doi.org/10.1016/j.cell.2017.05.023

Audette, N.J., Zhou, W., Schneider, D.M., 2021. Temporally precise movement-based predictions in the mouse auditory cortex. https://doi.org/10.1101/2021.12.13.472457

Ayaz, A., Stäuble, A., Hamada, M., Wulf, M.A., Saleem, A.B., Helmchen, F., 2019. Layer-specific integration of locomotion and sensory information in mouse barrel cortex. Nature Communications 10, 1–14. https://doi.org/10.1038/s41467-019-10564-8

Bastos, A.M., Usrey, W.M., Adams, R.A., Mangun, G.R., Fries, P., Friston, K.J., 2012. Canonical microcircuits for predictive coding. Neuron 76, 695–711. https://doi.org/10.1016/j.neuron.2012.10.038

Catafau, A.M., Parellada, E., Lomeña, F.J., Bernardo, M., Pavía, J., Ros, D., Setoain, J., Gonzalez-Monclús, E., 1994. Prefrontal and temporal blood flow in schizophrenia: resting and activation technetium-99m-HMPAO SPECT patterns in young neuroleptic-naive patients with acute disease. J Nucl Med 35, 935–941.

Chan, K.Y., Jang, M.J., Yoo, B.B., Greenbaum, A., Ravi, N., Wu, W.-L., Sánchez-Guardado, L., Lois, C., Mazmanian, S.K., Deverman, B.E., Gradinaru, V., 2017. Engineered AAVs for efficient noninvasive gene delivery to the central and peripheral nervous systems. Nat Neurosci 20, 1172–1179. https://doi.org/10.1038/nn.4593

Chen, X., Sun, Y.-C., Zhan, H., Kebschull, J.M., Fischer, S., Matho, K., Huang, Z.J., Gillis, J., Zador, A.M., 2019. High-Throughput Mapping of Long-Range Neuronal Projection Using In Situ Sequencing. Cell 179, 772-786.e19. https://doi.org/10.1016/j.cell.2019.09.023

Constantinople, C.M., Bruno, R.M., 2013. Deep cortical layers are activated directly by thalamus. Science (New York, N.Y.) 340, 1591–1594. https://doi.org/10.1126/science.1236425

Daigle, T.L., Madisen, L., Hage, T.A., Valley, M.T., Knoblich, U., Larsen, R.S., Takeno, M.M., Huang, L., Gu, H., Larsen, R., Mills, M., Bosma-Moody, A., Siverts, L.A., Walker, M., Graybuck, L.T., Yao, Z., Fong, O., Nguyen, T.N., Garren, E., Lenz, G.H., Chavarha, M., Pendergraft, J., Harrington, J., Hirokawa, K.E., Harris, J.A., Nicovich, P.R., McGraw, M.J., Ollerenshaw, D.R., Smith, K.A., Baker, C.A., Ting, J.T., Sunkin, S.M., Lecoq, J., Lin, M.Z., Boyden, E.S., Murphy, G.J., da Costa, N.M., Waters, J., Li, L., Tasic, B., Zeng, H., 2018. A Suite of Transgenic Driver and Reporter Mouse Lines with Enhanced Brain-Cell-Type Targeting and Functionality. Cell 174, 465-480.e22. https://doi.org/10.1016/j.cell.2018.06.035

Dierks, T., Linden, D.E., Jandl, M., Formisano, E., Goebel, R., Lanfermann, H., Singer, W., 1999. Activation of Heschl's gyrus during auditory hallucinations. Neuron 22, 615–621. https://doi.org/10.1016/s0896-6273(00)80715-1

Dombeck, Daniel A., Khabbaz, A.N., Collman, F., Adelman, T.L., Tank, D.W., 2007. Imaging large-scale neural activity with cellular resolution in awake, mobile mice. Neuron 56, 43–57. https://doi.org/10.1016/j.neuron.2007.08.003

Dombeck, Daniel A, Khabbaz, A.N., Collman, F., Adelman, T.L., Tank, D.W., 2007. Imaging large-scale neural activity with cellular resolution in awake, mobile mice. Neuron 56, 43–57. https://doi.org/10.1016/j.neuron.2007.08.003

Douglas, R.J., Martin, K.A., 1991. A functional microcircuit for cat visual cortex. The Journal of Physiology 440, 735–769. https://doi.org/10.1113/jphysiol.1991.sp018733

Du, J., Palaniyappan, L., Liu, Z., Cheng, W., Gong, W., Zhu, M., Wang, J., Zhang, J., Feng, J., 2021. The genetic determinants of language network dysconnectivity in drug-naïve early stage schizophrenia. NPJ Schizophr 7, 18. https://doi.org/10.1038/s41537-021-00141-8

Eliades, S.J., Wang, X., 2008. Neural substrates of vocalization feedback monitoring in primate auditory cortex. Nature 453, 1102–6. https://doi.org/10.1038/nature06910

Fletcher, P.C., Frith, C.D., 2009. Perceiving is believing: a Bayesian approach to explaining the positive symptoms of schizophrenia. Nature reviews. Neuroscience 10, 48–58. https://doi.org/10.1038/nrn2536

Franco, S.J., Gil-Sanz, C., Martinez-Garay, I., Espinosa, A., Harkins-Perry, S.R., Ramos, C., Müller, U., 2012. Fate-Restricted Neural Progenitors in the Mammalian Cerebral Cortex. Science. https://doi.org/10.1126/science.1223616

Frith, C., 2005. The neural basis of hallucinations and delusions. Comptes rendus biologies 328, 169–75.

Garner, A.R., Keller, G.B., 2022. A cortical circuit for audio-visual predictions. Nat Neurosci 25, 98–105. https://doi.org/10.1038/s41593-021-00974-7

Gerfen, C.R., Paletzki, R., Heintz, N., 2013. GENSAT BAC Cre-Recombinase Driver Lines to Study the Functional Organization of Cerebral Cortical and Basal Ganglia Circuits. Neuron 80, 1368–1383. https://doi.org/10.1016/j.neuron.2013.10.016

Gong, S., Doughty, M., Harbaugh, C.R., Cummins, A., Hatten, M.E., Heintz, N., Gerfen, C.R., 2007. Targeting Cre Recombinase to Specific Neuron Populations with Bacterial Artificial Chromosome Constructs. J. Neurosci. 27, 9817–9823.

Gorski, J.A., Talley, T., Qiu, M., Puelles, L., Rubenstein, J.L.R., Jones, K.R., 2002. Cortical excitatory neurons and glia, but not GABAergic neurons, are produced in the Emx1-expressing lineage. J Neurosci 22, 6309–6314. https://doi.org/20026564

Guo, Z.V., Li, N., Huber, D., Ophir, E., Gutnisky, D., Ting, J.T., Feng, G., Svoboda, K., 2014. Flow of cortical activity underlying a tactile decision in mice. Neuron 81, 179–194. https://doi.org/10.1016/j.neuron.2013.10.020

Haarsma, J., Kok, P., Browning, M., 2020. The promise of layer-specific neuroimaging for testing predictive coding theories of psychosis. Schizophrenia Research. https://doi.org/10.1016/j.schres.2020.10.009

Harris, J.A., Mihalas, S., Hirokawa, K.E., Whitesell, J.D., Choi, H., Bernard, A., Bohn, P., Caldejon, S., Casal, L., Cho, A., Feiner, A., Feng, D., Gaudreault, N., Gerfen, C.R., Graddis, N., Groblewski, P.A., Henry, A.M., Ho, A., Howard, R., Knox, J.E., Kuan, L., Kuang, X., Lecoq, J., Lesnar, P., Li, Y., Luviano, J., McConoughey, S., Mortrud, M.T., Naeemi, M., Ng, L., Oh, S.W., Ouellette, B., Shen, E., Sorensen, S.A., Wakeman, W., Wang, Q., Wang, Y., Williford, A., Phillips, J.W., Jones, A.R., Koch, C., Zeng, H., 2019. Hierarchical organization of cortical and thalamic connectivity. Nature 575, 195–202. https://doi.org/10.1038/s41586-019-1716-z

Harrison, P.J., Weinberger, D.R., 2005. Schizophrenia genes, gene expression, and neuropathology: on the matter of their convergence. Mol Psychiatry 10, 40–68. https://doi.org/10.1038/sj.mp.4001558

Heindorf, M., Arber, S., Keller, G.B., 2018. Mouse Motor Cortex Coordinates the Behavioral Response to Unpredicted Sensory Feedback. Neuron 99, 1040-1054.e5. https://doi.org/10.1016/j.neuron.2018.07.046

Hippenmeyer, S., Vrieseling, E., Sigrist, M., Portmann, T., Laengle, C., Ladle, D.R., Arber, S., 2005. A Developmental Switch in the Response of DRG Neurons to ETS Transcription Factor Signaling. PLOS Biology 3, e159. https://doi.org/10.1371/journal.pbio.0030159

Javitt, D.C., 2009. Sensory Processing in Schizophrenia: Neither Simple nor Intact. Schizophr Bull 35, 1059–1064. https://doi.org/10.1093/schbul/sbp110

Jiang, L.P., Rao, R.P.N., 2021. Predictive Coding Theories of Cortical Function. arXiv:2112.10048 [q-bio].

Jordan, M.I., Rumelhart, D.E., 1992. Forward Models: Supervised Learning with a Distal Teacher. Cognitive Science 16, 307–354. https://doi.org/10.1207/s15516709cog1603_1

Jordan, R., Keller, G.B., 2020. Opposing Influence of Top-down and Bottom-up Input on Excitatory Layer 2/3 Neurons in Mouse Primary Visual Cortex. Neuron 108, 1194-1206.e5. https://doi.org/10.1016/j.neuron.2020.09.024

Keller, G.B., Bonhoeffer, T., Hübener, M., 2012. Sensorimotor mismatch signals in primary visual cortex of the behaving mouse. Neuron 74, 809–15. https://doi.org/10.1016/j.neuron.2012.03.040

Keller, G.B., Hahnloser, R.H.R., 2009. Neural processing of auditory feedback during vocal practice in a songbird. Nature 457, 187–90. https://doi.org/10.1038/nature07467

Keller, G.B., Mrsic-Flogel, T.D., 2018. Predictive Processing: A Canonical Cortical Computation. Neuron 100, 424–435. https://doi.org/10.1016/j.neuron.2018.10.003

Kim, T.H., Zhang, Y., Lecoq, J., Jung, J.C., Li, J., Zeng, H., Niell, C.M., Schnitzer, M.J., 2016. Long-Term Optical Access to an Estimated One Million Neurons in the Live Mouse Cortex. Cell Rep 17, 3385–3394. https://doi.org/10.1016/j.celrep.2016.12.004

Kiritani, T., Wickersham, I.R., Seung, H.S., Shepherd, G.M.G., 2012. Hierarchical connectivity and connection-specific dynamics in the corticospinal-corticostriatal microcircuit in mouse motor cortex. J Neurosci 32, 4992–5001. https://doi.org/10.1523/JNEUROSCI.4759-11.2012

Le Bihan, D., Turner, R., Zeffiro, T.A., Cuénod, C.A., Jezzard, P., Bonnerot, V., 1993. Activation of human primary visual cortex during visual recall: a magnetic resonance imaging study. Proceedings of the National Academy of Sciences of the United States of America 90, 11802–5.

Leinweber, M., Ward, D.R., Sobczak, J.M., Attinger, A., Keller, G.B., 2017. A Sensorimotor Circuit in Mouse Cortex for Visual Flow Predictions. Neuron 95, 1420-1432.e5. https://doi.org/10.1016/j.neuron.2017.08.036

Leinweber, M., Zmarz, P., Buchmann, P., Argast, P., Hübener, M., Bonhoeffer, T., Keller, G.B., 2014. Two-photon calcium imaging in mice navigating a virtual reality environment. Journal of visualized experiments : JoVE e50885.

Li, T., Wang, Q., Zhang, J., Rolls, E.T., Yang, W., Palaniyappan, L., Zhang, L., Cheng, W., Yao, Y., Liu, Zhaowen, Gong, X., Luo, Q., Tang, Y., Crow, T.J., Broome, M.R., Xu, K., Li, C., Wang, J., Liu, Zhening, Lu, G., Wang, F., Feng, J., 2017. Brain-Wide Analysis of Functional Connectivity in First-Episode and Chronic Stages of Schizophrenia. Schizophr Bull 43, 436–448. https://doi.org/10.1093/schbul/sbw099

Ma, Y., Shaik, M.A., Kim, S.H., Kozberg, M.G., Thibodeaux, D.N., Zhao, H.T., Yu, H., Hillman, E.M.C., 2016. Wide-field optical mapping of neural activity and brain haemodynamics: considerations and novel approaches. Philosophical Transactions of the Royal Society B: Biological Sciences 371, 20150360. https://doi.org/10.1098/rstb.2015.0360

1113 Madisen, L., Zwingman, T.A., Sunkin, S.M., Oh, S.W., Zariwala, H.A., Gu, H., Ng, L.L., Palmiter, R.D.,
1114 Hawrylycz, M.J., Jones, A.R., Lein, E.S., Zeng, H., 2010. A robust and high-throughput Cre
1115 reporting and characterization system for the whole mouse brain. Nature Neuroscience 13,
1116 133–140. https://doi.org/10.1038/nn.2467
1117 Maia, T.V., Frank, M.J., 2017. An Integrative Perspective on the Role of Dopamine in Schizophrenia.
1118 Biol Psychiatry 81, 52–66. https://doi.org/10.1016/j.biopsych.2016.05.021
1119 Moghaddam, B., Javitt, D., 2012. From Revolution to Evolution: The Glutamate Hypothesis of
1120 Schizophrenia and its Implication for Treatment. Neuropsychopharmacol 37, 4–15.
1121 https://doi.org/10.1038/npp.2011.181
1122 Morita, K., Im, S., Kawaguchi, Y., 2019. Differential Striatal Axonal Arborizations of the
1123 Intratelencephalic and Pyramidal-Tract Neurons: Analysis of the Data in the MouseLight
1124 Database. Frontiers in Neural Circuits 13.
1125 Musall, S., Kaufman, M.T., Juavinett, A.L., Gluf, S., Churchland, A.K., 2019. Single-trial neural
1126 dynamics are dominated by richly varied movements. Nat Neurosci 22, 1677–1686.
1127 https://doi.org/10.1038/s41593-019-0502-4
1128 Northoff, G., Duncan, N.W., 2016. How do abnormalities in the brain's spontaneous activity translate
1129 into symptoms in schizophrenia? From an overview of resting state activity findings to a
1130 proposed spatiotemporal psychopathology. Prog Neurobiol 145–146, 26–45.
1131 https://doi.org/10.1016/j.pneurobio.2016.08.003
1132 Oberlaender, M., Ramirez, A., Bruno, R.M., 2012. Sensory Experience Restructures Thalamocortical
1133 Axons during Adulthood. Neuron 74, 648–655.
1134 https://doi.org/10.1016/j.neuron.2012.03.022
1135 Pakan, J.M., Lowe, S.C., Dylda, E., Keemink, S.W., Currie, S.P., Coutts, C.A., Rochefort, N.L., 2016.
1136 Behavioral-state modulation of inhibition is context-dependent and cell type specific in
1137 mouse visual cortex. eLife 5. https://doi.org/10.7554/eLife.14985
1138 Parellada, M., Gomez-Vallejo, S., Burdeus, M., Arango, C., 2017. Developmental Differences Between
1139 Schizophrenia and Bipolar Disorder. Schizophr Bull 43, 1176–1189.
1140 https://doi.org/10.1093/schbul/sbx126
1141 Rao, R.P.N., Ballard, D.H., 1999. Predictive coding in the visual cortex: a functional interpretation of
1142 some extra-classical receptive-field effects. Nature Neuroscience 2, 79–87.
1143 https://doi.org/10.1038/4580
1144 Saleem, A.B., Ayaz, A., Jeffery, K.J., Harris, K.D., Carandini, M., 2013. Integration of visual motion and
1145 locomotion in mouse visual cortex. Nature neuroscience 16, 1864–9.
1146 https://doi.org/10.1038/nn.3567
1147 Saravanan, V., Berman, G.J., Sober, S.J., 2020. Application of the hierarchical bootstrap to multi-level
1148 data in neuroscience. Neuron Behav Data Anal Theory 3,
1149 https://nbdt.scholasticahq.com/article/13927-application-of-the-hierarchical-bootstrap-to-
1150 multi-level-data-in-neuroscience.
1151 Schmack, K., Bosc, M., Ott, T., Sturgill, J.F., Kepecs, A., 2021. Striatal dopamine mediates
1152 hallucination-like perception in mice. Science 372, eabf4740.
1153 https://doi.org/10.1126/science.abf4740
1154 Schneider, D.M., Sundararajan, J., Mooney, R., 2018. A cortical filter that learns to suppress the
1155 acoustic consequences of movement. Nature 561, 391–395.
1156 https://doi.org/10.1038/s41586-018-0520-5
1157 Shergill, S.S., Brammer, M.J., Williams, S.C., Murray, R.M., McGuire, P.K., 2000. Mapping auditory
1158 hallucinations in schizophrenia using functional magnetic resonance imaging. Arch Gen
1159 Psychiatry 57, 1033–1038. https://doi.org/10.1001/archpsyc.57.11.1033
1160 Singh, T., Neale, B.M., Daly, M.J., Consortium, on behalf of the S.E.M.-A. (SCHEMA), 2020. Exome
1161 sequencing identifies rare coding variants in 10 genes which confer substantial risk for
1162 schizophrenia. https://doi.org/10.1101/2020.09.18.20192815

Stanley, J., Miall, R.C., 2007. Functional activation in parieto-premotor and visual areas dependent on congruency between hand movement and visual stimuli during motor-visual priming. NeuroImage 34, 290–9. https://doi.org/10.1016/j.neuroimage.2006.08.043

Stringer, C., Pachitariu, M., Steinmetz, N., Reddy, C.B., Carandini, M., Harris, K.D., 2019. Spontaneous behaviors drive multidimensional, brainwide activity. Science 364, 255. https://doi.org/10.1126/science.aav7893

Suzuki, M., Larkum, M.E., 2020. General Anesthesia Decouples Cortical Pyramidal Neurons. Cell 180, 666-676.e13. https://doi.org/10.1016/j.cell.2020.01.024

Taniguchi, H., He, M., Wu, P., Kim, S., Paik, R., Sugino, K., Kvitsani, D., Fu, Y., Lu, J., Lin, Y., Miyoshi, G., Shima, Y., Fishell, G., Nelson, S.B., Huang, Z.J., 2011. A Resource of Cre Driver Lines for Genetic Targeting of GABAergic Neurons in Cerebral Cortex. Neuron 71, 995–1013. https://doi.org/10.1016/j.neuron.2011.07.026

Valley, M.T., Moore, M.G., Zhuang, J., Mesa, N., Castelli, D., Sullivan, D., Reimers, M., Waters, J., 2020. Separation of hemodynamic signals from GCaMP fluorescence measured with wide-field imaging. J Neurophysiol 123, 356–366. https://doi.org/10.1152/jn.00304.2019

Wekselblatt, J.B., Flister, E.D., Piscopo, D.M., Niell, C.M., 2016. Large-scale imaging of cortical dynamics during sensory perception and behavior. Journal of Neurophysiology 115, 2852–2866. https://doi.org/10.1152/jn.01056.2015

Widmer, F.C., Keller, G.B., 2021. Developmental plasticity in visual cortex is necessary for normal visuomotor integration and visuomotor skill learning. bioRxiv 2021.06.20.449148. https://doi.org/10.1101/2021.06.20.449148

Xu, X., Olivas, N.D., Ikrar, T., Peng, T., Holmes, T.C., Nie, Q., Shi, Y., 2016. Primary visual cortex shows laminar-specific and balanced circuit organization of excitatory and inhibitory synaptic connectivity. The Journal of Physiology 594, 1891–1910. https://doi.org/10.1113/JP271891

Yamawaki, N., Shepherd, G.M.G., 2015. Synaptic circuit organization of motor corticothalamic neurons. J Neurosci 35, 2293–2307. https://doi.org/10.1523/JNEUROSCI.4023-14.2015

Yoon, J.H., Rokem, A.S., Silver, M.A., Minzenberg, M.J., Ursu, S., Ragland, J.D., Carter, C.S., 2009. Diminished orientation-specific surround suppression of visual processing in schizophrenia. Schizophr Bull 35, 1078–1084. https://doi.org/10.1093/schbul/sbp064

Zmarz, P., Keller, G.B., 2016. Mismatch Receptive Fields in Mouse Visual Cortex. Neuron 92, 766–772. https://doi.org/10.1016/j.neuron.2016.09.057